APPENDIX A Ultrasonic Interaction With Thin Layers

A.1 Single Interface

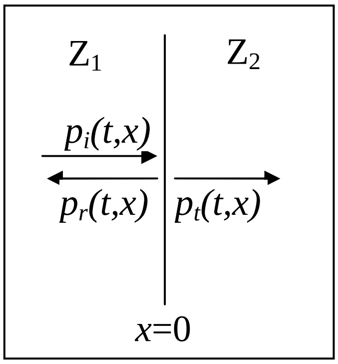

Z	Acoustic Impedance
p	Acoustic Pressure
u	Particle Velocity
A	Pressure Amplitude at x = 0
I	Intensity
R	Intensity Reflection Coefficient
T	Intensity Transmission Coefficient
r	Pressure Reflection Coefficient
t	Pressure Transmission Coefficient
α_1 α_2	Attenuation Coefficient (nepers/m) in medium 1, 2
k_1 k_2	Wavenumber ($2\pi f/c$) in medium 1, 2

$$p_i(t,x) = A_i e^{i(\omega t - k_1 x) - \alpha_1 x} \qquad I = pu$$

$$p_r(t,x) = A_r e^{i(\omega t + k_1 x) + \alpha_1 x} \qquad u = p / Z \text{ (for plane waves)}$$

$$p_t(t,x) = A_t e^{i(\omega t - k_2 x) - \alpha_2 x} \qquad I = p^2 / Z \text{ (for plane waves)}$$

$$A_r = rA_i \qquad A_t = tA_i$$

For normal incidence plane waves at a single interface, the following treatment for reflection and transmission applies:

$$r = \frac{Z_2 - Z_1}{Z_2 + Z_1} \qquad R = \frac{(Z_2 - Z_1)^2}{(Z_2 + Z_1)^2}$$

$$t = \frac{2Z_2}{Z_2 + Z_1} \qquad T = \frac{4Z_2 Z_1}{(Z_2 + Z_1)^2} \text{ because } \frac{I_t}{I_i} = \frac{A_t^2 / Z_2}{A_i^2 / Z_1} = \frac{A_t^2 Z_1}{A_i^2 Z_2}$$

A.2 Dual Interface – Thin Layer

r_{12} Pressure Reflection Coeff. Interface 1-2

t_{12} Pressure Transmission Coeff Interface 1-2

r_{21} Pressure Reflection Coeff. Interface 2-1

t_{21} Pressure Transmission Coeff Interface 2-1

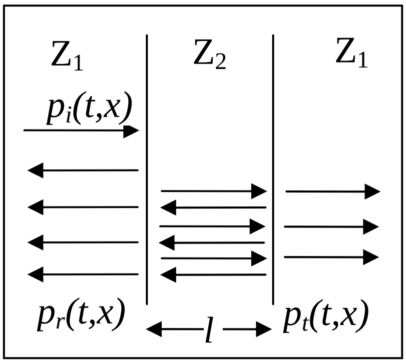

$$r_{12} = \frac{Z_2 - Z_1}{Z_2 + Z_1} \qquad t_{12} = \frac{2Z_2}{Z_2 + Z_1}$$

$$r_{21} = \frac{Z_1 - Z_2}{Z_2 + Z_1} \qquad t_{21} = \frac{2Z_1}{Z_2 + Z_1}$$

For normal incidence plane waves at a dual interface, the following treatment for reflection and transmission applies.

Multiple reflections between the two interfaces result in Geometric Progressions for the overall reflection and transmission coefficients:

$$r = r_{12} + t_{12}t_{21}r_{21}e^{-2l(ik_2+\alpha_2)}\sum_{n=0}^{\infty}\left[r_{21}^2 e^{-2l(ik_2+\alpha_2)}\right]^n$$

$$t = t_{12}t_{21}\sum_{n=0}^{\infty}\left[r_{21}^2 e^{-2l(ik_2+\alpha_2)}\right]^n$$

As $r_{21} = -r_{12}$ then:

$$r = r_{12}\left\{1 - t_{12}t_{21}e^{-2l(ik_2+\alpha_2)}\sum_{n=0}^{\infty}\left[r_{12}^2 e^{-2l(ik_2+\alpha_2)}\right]^n\right\}$$

$$t = t_{12}t_{21}\sum_{n=0}^{\infty}\left[r_{12}^2 e^{-2l(ik_2+\alpha_2)}\right]^n$$

Finally, assuming that $-1 < r_{12} < 1$ so that the GP converges, and by summing the GP to infinity in each case:

$$r = r_{12}\left[1 - \frac{t_{12}t_{21}e^{-2l(ik_2+\alpha_2)}}{1 - r_{12}^2 e^{-2l(ik_2+\alpha_2)}}\right] \qquad \text{(A-1)}$$

$$t = \frac{t_{12}t_{21}}{1 - r_{12}^2 e^{-2l(ik_2+\alpha_2)}} \qquad \text{(A-2)}$$

A.2.1 Calculating the reflection coefficient: r

$$r = r_{12}\left[\frac{1-(r_{12}^2 + t_{12}t_{21})e^{-2l(ik_2+\alpha_2)}}{1 - r_{12}^2 e^{-2l(ik_2+\alpha_2)}}\right]$$

It can be shown that: $r_{12}^2 + t_{12}t_{21} = 1$. Hence:

$$r = r_{12}\left[\frac{1 - e^{-2l(ik_2+\alpha_2)}}{1 - r_{12}^2 e^{-2l(ik_2+\alpha_2)}}\right]$$

In order to determine the modulus of the reflection coefficient:

$$\frac{|r|^2}{r_{12}^2} = \frac{\left(1 - e^{-2\alpha_2 l}\cos 2k_2 l\right)^2 + e^{-4\alpha_2 l}\sin^2 2k_2 l}{(1 - r_{12}^2 e^{-2\alpha_2 l}\cos 2k_2 l)^2 + r_{12}^4 e^{-4\alpha_2 l}\sin^2 2k_2 l}$$

$$\frac{|r|^2}{r_{12}^2} = \frac{1 + e^{-4\alpha_2 l} - 2e^{-2\alpha_2 l}\cos 2k_2 l}{1 + r_{12}^4 e^{-4\alpha_2 l} - 2r_{12}^2 e^{-2\alpha_2 l}\cos 2k_2 l}$$

Using $\cos 2k_2 l = 1 - 2\sin^2 k_2 l$:

$$\frac{|r|^2}{r_{12}^2} = \frac{1 + e^{-4\alpha_2 l} - 2e^{-2\alpha_2 l} + 4e^{-2\alpha_2 l}\sin^2 k_2 l}{1 + r_{12}^4 e^{-4\alpha_2 l} - 2r_{12}^2 e^{-2\alpha_2 l} + 4r_{12}^2 e^{-2\alpha_2 l}\sin^2 k_2 l}$$

$$\frac{|r|^2}{r_{12}^2} = \frac{\left(1 - e^{-2\alpha_2 l}\right)^2 + 4e^{-2\alpha_2 l}\sin^2 k_2 l}{\left(1 - r_{12}^2 e^{-2\alpha_2 l}\right)^2 + 4r_{12}^2 e^{-2\alpha_2 l}\sin^2 k_2 l}$$

$$\frac{|r|^2}{r_{12}^2} = \frac{\left(1 - e^{-2\alpha_2 l}\right)^2 \sec^2 k_2 l + 4e^{-2\alpha_2 l}\tan^2 k_2 l}{\left(1 - r_{12}^2 e^{-2\alpha_2 l}\right)^2 \sec^2 k_2 l + 4r_{12}^2 e^{-2\alpha_2 l}\tan^2 k_2 l}$$

$$\frac{|r|^2}{r_{12}^2} = \frac{\left(1 - e^{-2\alpha_2 l}\right)^2\left(1 + \tan^2 k_2 l\right) + 4e^{-2\alpha_2 l}\tan^2 k_2 l}{\left(1 - r_{12}^2 e^{-2\alpha_2 l}\right)^2\left(1 + \tan^2 k_2 l\right) + 4r_{12}^2 e^{-2\alpha_2 l}\tan^2 k_2 l}$$

$$\frac{|r|^2}{r_{12}^2} = \frac{\left(1 - e^{-2\alpha_2 l}\right)^2 + \left(1 + e^{-2\alpha_2 l}\right)^2\tan^2 k_2 l}{\left(1 - r_{12}^2 e^{-2\alpha_2 l}\right)^2 + \left(1 + r_{12}^2 e^{-2\alpha_2 l}\right)^2\tan^2 k_2 l} \qquad \text{(A-3)}$$

If attenuation in the inter-layer is neglected (ie $\alpha_2 = 0$), then:

$$\frac{|r|^2}{r_{12}^2} = \frac{4\tan^2 k_2 l}{\left(1 - r_{12}^2\right)^2 + \left(1 + r_{12}^2\right)^2 \tan^2 k_2 l}$$

$$\frac{|r|^2}{r_{12}^2} = \frac{4(Z_2 + Z_1)^4 \tan^2 k_2 l}{\left[(Z_2 + Z_1)^2 - (Z_2 - Z_1)^2\right]^2 + \left[(Z_2 + Z_1)^2 + (Z_2 - Z_1)^2\right]^2 \tan^2 k_2 l}$$

$$|r| = \frac{\left|(Z_2 - Z_1)(Z_2 + Z_1)\tan k_2 l\right|}{\sqrt{4Z_2^2 Z_1^2 + \left(Z_2^2 + Z_1^2\right)^2 \tan^2 k_2 l}} \qquad \textit{(A-4)}$$

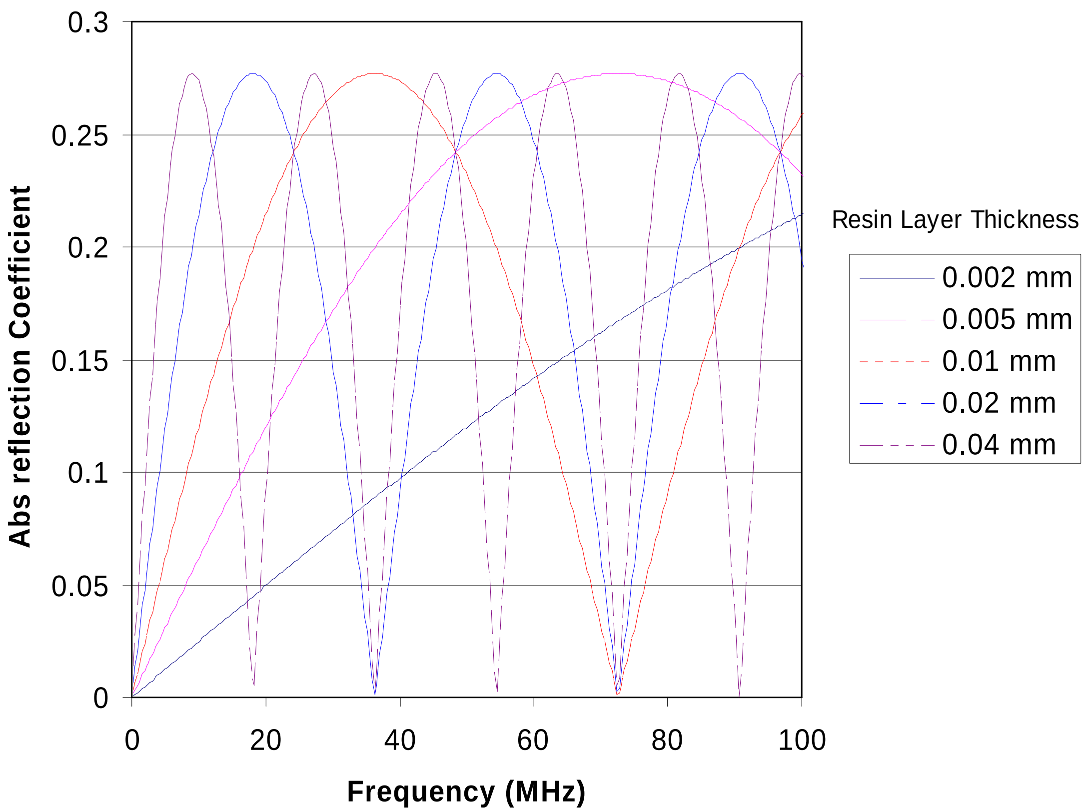

Figure A-1. Plot of the absolute reflection coefficient from equation A-4 using a single thin resin layer embedded in carbon-fibre composite of 80% fibre volume fraction. This becomes the modulation function for inter-ply resonances.

A.2.2 Calculating the transmission coefficient: t

From Equation (A-1):

$$t = \frac{t_{12}t_{21}}{1 - r_{12}^2 e^{-2\alpha_2 l}\left(\cos 2k_2 l - i\sin 2k_2 l\right)}$$

$$|t|^2 = \frac{\left(t_{12}t_{21}\right)^2}{\left(1 - r_{12}^2 e^{-2\alpha_2 l}\cos 2k_2 l\right)^2 + r_{12}^4 e^{-4\alpha_2 l}\sin^2 2k_2 l}$$

$$|t|^2 = \frac{\left(t_{12}t_{21}\right)^2}{1 - 2r_{12}^2 e^{-2\alpha_2 l}\cos 2k_2 l + r_{12}^4 e^{-4\alpha_2 l}}$$

$$|t|^2 = \frac{\left(t_{12}t_{21}\right)^2}{1 - 2r_{12}^2 e^{-2\alpha_2 l}\left(1 - 2\sin^2 k_2 l\right) + r_{12}^4 e^{-4\alpha_2 l}}$$

$$|t|^2 = \frac{\left(t_{12}t_{21}\right)^2}{\left(1 - r_{12}^2 e^{-2\alpha_2 l}\right)^2 + 4r_{12}^2 e^{-2\alpha_2 l}\sin^2 k_2 l}$$

$$|t|^2 = \frac{\left(4Z_1Z_2\right)^2}{\left[\left(Z_2+Z_1\right)^2 - \left(Z_2-Z_1\right)^2 e^{-2\alpha_2 l}\right]^2 + 4\left(Z_2-Z_1\right)^2\left(Z_2+Z_1\right)^2 e^{-2\alpha_2 l}\sin^2 k_2 l}$$

$$|t|^2 = \frac{\left(4Z_1Z_2\right)^2}{\left[\left(Z_2+Z_1\right) - \left(Z_2-Z_1\right)e^{-\alpha_2 l}\right]^2\left[\left(Z_2+Z_1\right) + \left(Z_2-Z_1\right)e^{-\alpha_2 l}\right]^2 + 4\left(Z_2-Z_1\right)^2\left(Z_2+Z_1\right)^2 e^{-2\alpha_2 l}\sin^2 k_2 l}$$

$$|t|^2 = \frac{\left(4Z_1Z_2\right)^2}{\left[Z_1\left(1+e^{-\alpha_2 l}\right) + Z_2\left(1-e^{-\alpha_2 l}\right)\right]^2\left[Z_1\left(1-e^{-\alpha_2 l}\right) + Z_2\left(1+e^{-\alpha_2 l}\right)\right]^2 + 4\left(Z_2-Z_1\right)^2\left(Z_2+Z_1\right)^2 e^{-2\alpha_2 l}\sin^2 k_2 l}$$

If attenuation in the inter-layer is neglected (ie $\alpha_2 = 0$), then:

$$|t|^2 = \frac{\left(4Z_1Z_2\right)^2}{\left[2Z_1\right]^2\left[2Z_2\right]^2 + 4\left(Z_2-Z_1\right)^2\left(Z_2+Z_1\right)^2\sin^2 k_2 l}$$

$$|t|^2 = \frac{4Z_1^2Z_2^2}{4Z_1^2Z_2^2 + \left(Z_2-Z_1\right)^2\left(Z_2+Z_1\right)^2\sin^2 k_2 l}$$

$$|t| = \frac{2Z_1Z_2}{\sqrt{4Z_1^2Z_2^2 + \left(Z_2-Z_1\right)^2\left(Z_2+Z_1\right)^2\sin^2 k_2 l}} \qquad \text{(A-5)}$$

APPENDIX B Reflection and Transmission at a rough surface

For measurements of absolute attenuation to be corrected for surface losses it is necessary to be able to measure or calculate those surface losses accurately. This can be achieved in a variety of ways for smooth surfaces where the normal-incidence plane-wave reflection and transmission coefficients are independent of frequency. However, rough surfaces scatter ultrasound in a frequency-dependent manner and the transmission coefficient must be determined at the particular frequency used for the attenuation scan. Apart from the method of using a step wedge to obtain measurements at a range of thicknesses, the other methods of correcting for surface losses cannot easily provide this information. The following discussion includes an analysis of the problem and proposes another method for determining transmission coefficients at specific frequencies.

B.1 Smooth interfaces

At a smooth interface there should be minimal scattering and conservation of energy, which requires that the energy in the incident wave equals the sum of the energies in the reflected and transmitted waves. The intensity I is the average rate of flow of energy through unit area normal to the direction of wave propagation. It can be shown that the ratio of the reflected and incident intensities is given by:

$$\frac{I_r}{I_i} = r^2 \qquad \text{(B-1)}$$

and the ratio of transmitted and incident intensities is given by:

$$\frac{I_t}{I_i} = \frac{t^2 Z_i}{Z_t} \qquad \text{(B-2)}$$

where r is the amplitude reflection coefficient, t is the amplitude transmission coefficient, Z_i is the acoustic impedance of the incident material and Z_t is that of the transmission material .

B.2 Rough interfaces

At a rough interface there will be energy loss due to scattering. This effect increases as the frequency increases. A phase-screen approximation, presented by Nagy and Rose 1993 gave the losses relative to the amplitudes for a smooth interface as:

Reduction in reflection coefficient due to scattering = $342.7\dfrac{R_q{}^2 f^2}{c_i^2}\ (\text{dB})$ *(B-3)*

Reduction in transmission coefficient due to scattering = $85.67 R_q{}^2 f^2 \left(\dfrac{1}{c_t} - \dfrac{1}{c_i}\right)^2\ (\text{dB})$ *(B-4)*

where R_q is the *rms* roughness of the surface, f is the frequency, and c_i is the speed of sound in the incident material and c_t is the speed of sound in the transmission material. Hence at a water/composite interface c_i is the speed of sound in water and c_t is the speed of sound in composite.

Therefore, measurements of the reflection coefficient at the interface over a range of frequencies can be used to determine the *rms* roughness. The extrapolated value for 0 Hz will also provide a method for determining the surface losses for rough surfaces.

APPENDIX C Use of the analytical model for FVF measurement

C.1 Ply thickness

Using the simple analytical model described in Appendix A with the simple volumetric mixture rule, it can be shown that both frequencies and reflection coefficients at resonance are proportional to local ply-thickness changes and hence to local FVF. If the density and acoustic velocity in the plies remain constant when the ply thickness changes, the resonance frequency would change as shown in Figure C-1 for the scenarios tabulated in Table C-1. Material properties used were: fibre density 1.69 kg/dm^3 and modulus 16 GPa, resin density 1.27 kg/dm^3 and modulus 10.7 GPa.

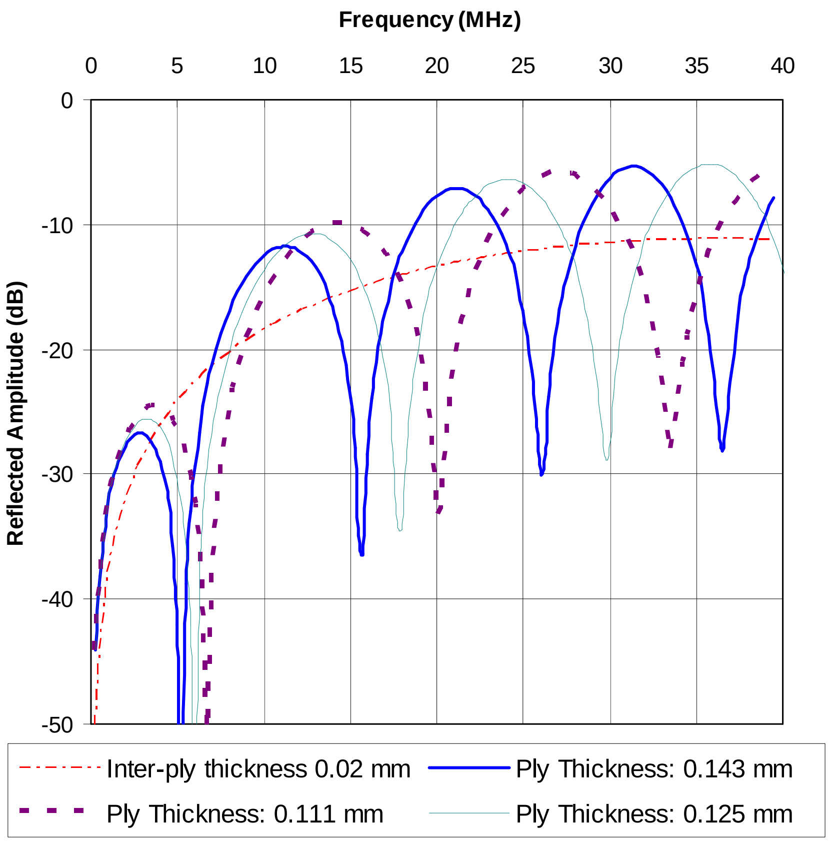

Figure C-1.Theoretical frequency response of a single ply with thickness corresponding to 7, 8 and 9 plies per mm, with the inter-ply layer reflection amplitude for a 0.02 mm layer shown too. The model assumed the same density and acoustic velocity for the plies regardless of ply thickness.

Ply Thickness (mm)	No. of plies	Total Thickness (mm)	Fibre Volume Fraction
0.143	7	1	80%
0.125	8	1	80%
0.111	9	1	80%

Table C-1. Values used for the modelled results shown in Figure C-1.

C.2 Fibre Volume Fraction (FVF)

If an assumption is made that fibres do not move laterally within a ply, then it follows that ply thickness changes are accompanied by corresponding FVF changes. Such local FVF changes are accompanied by changes in effective elastic moduli and density in the equivalent medium according to some mixture rule (see Chapter 4), thus causing a change in acoustic velocity. When these are taken into account in the simple propagation model, it is possible to calculate the change in frequency response as a result of FVF changes resulting from a ply changing in thickness. Figure C-2 shows the effect of varying the thickness of a ply that should normally be 0.125 mm thick with a FVF of 80%, but is allowed to change in thickness by approximately ±11%. The corresponding FVF changes are shown in Table C-2.

Ply Thickness (mm)	No. of plies	Total Thickness (mm)	Fibre Volume Fraction
0.143	7	1	70%
0.125	8	1	80%
0.111	9	1	90%

Table C-2. Values used for the modelled results shown in Figure C-2.

There are only imperceptible differences between the graphs in Figure C-1 and Figure C-2 because the velocity only varies by approximately 3% when the FVF increases from 70% to 90%. Thus the peak frequencies were only in error in Figure C-1 by 0.15 MHz.

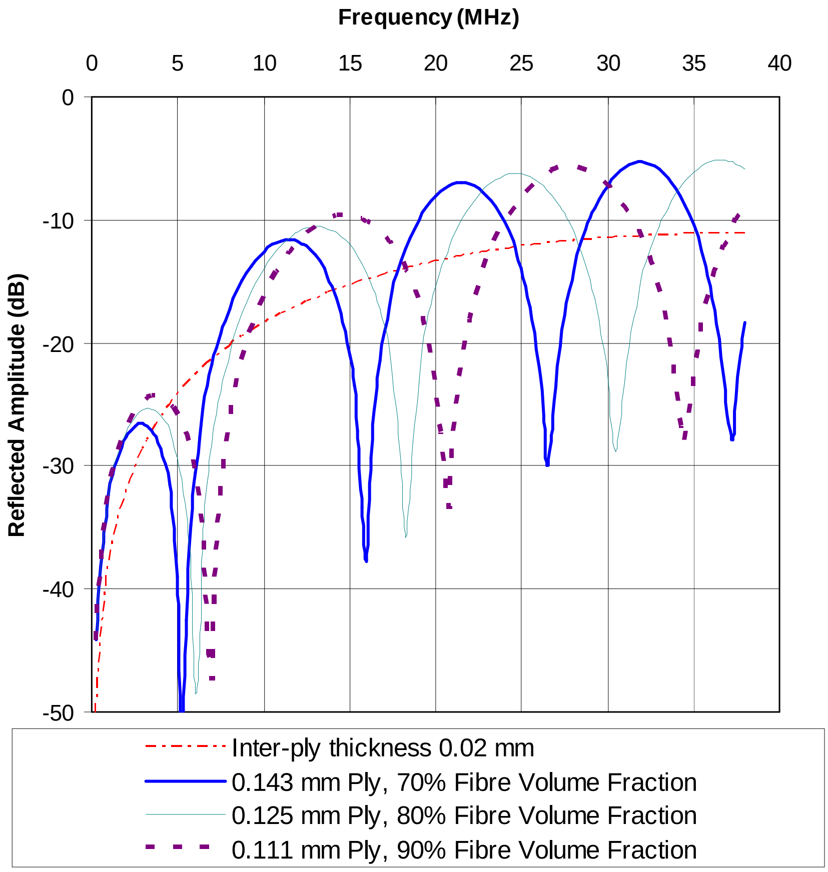

Figure C-2. Similar to Figure C-1 but allowing for density and modulus changes due to the FVF change associated with a ply varying in thickness. Theoretical frequency response of the ply resonance is shown for ply thickness variations of a ply that is nominally 0.125 mm thick at 80% FVF. The variation corresponds to a change from 70% FVF (0.143 mm thickness) through 80% FVF to 90% FVF (0.111 mm thickness).

As some of the specimens supplied for evaluating the strategy use plies as thick as 1 mm, a table and graphs have been produced (see Table C-3 and Figure C-3) to show the frequency dependence of the ply resonances in that case. Note that the resonances occur at much lower frequencies.

Ply Thickness (mm)	No. of plies	Total Thickness (mm)	Fibre Volume Fraction
1.143	7	8	70%
1.000	8	8	80%
0.889	9	8	90%

Table C-3. Values used for the modelled results shown in Figure C-3.

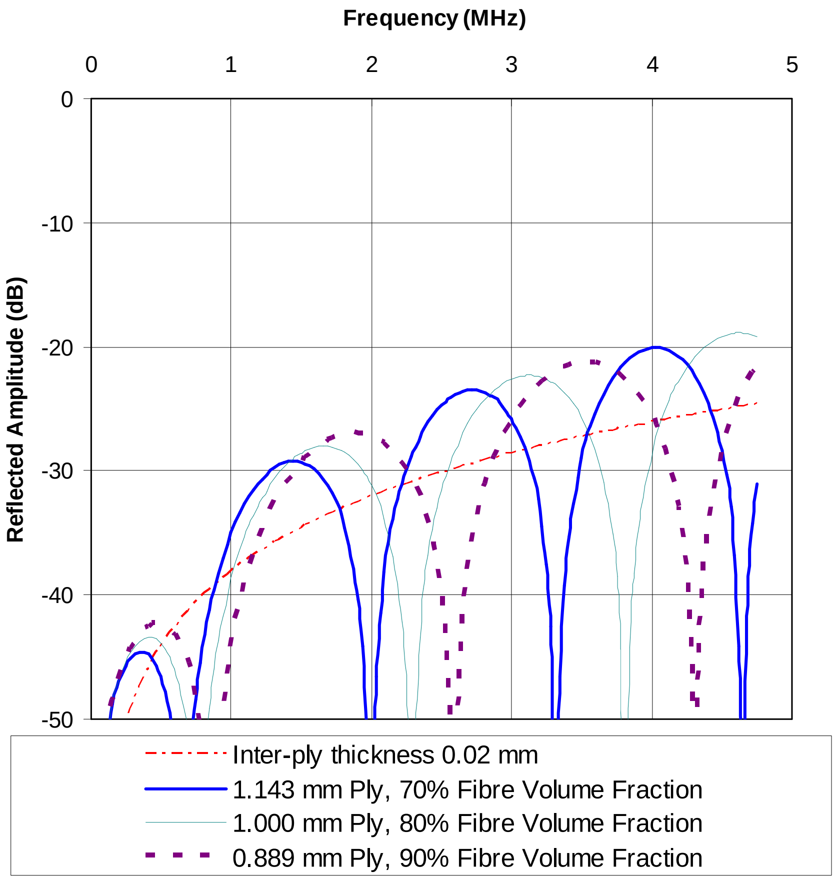

Figure C-3. Similar to Figure C-2 but for much thicker plies - nominally 1.0 mm thick at 80% FVF. The variation corresponds to a change from 70% FVF (1.143 mm thickness) through 80% FVF to 90% FVF (0.889 mm thickness).

By tracking the ply resonances from each volume element in the structure, it should be possible to obtain a measure of the local FVF. In order to use this it would be necessary to calibrate an ultrasonic parameter against FVF. There are two possible parameters: peak frequency or peak amplitude (reflection coefficient). These are both plotted against FVF in Figure C-4, Figure C-5 and Figure C-6 for material with 8 plies, 4 plies, and 1 ply per millimetre respectively.

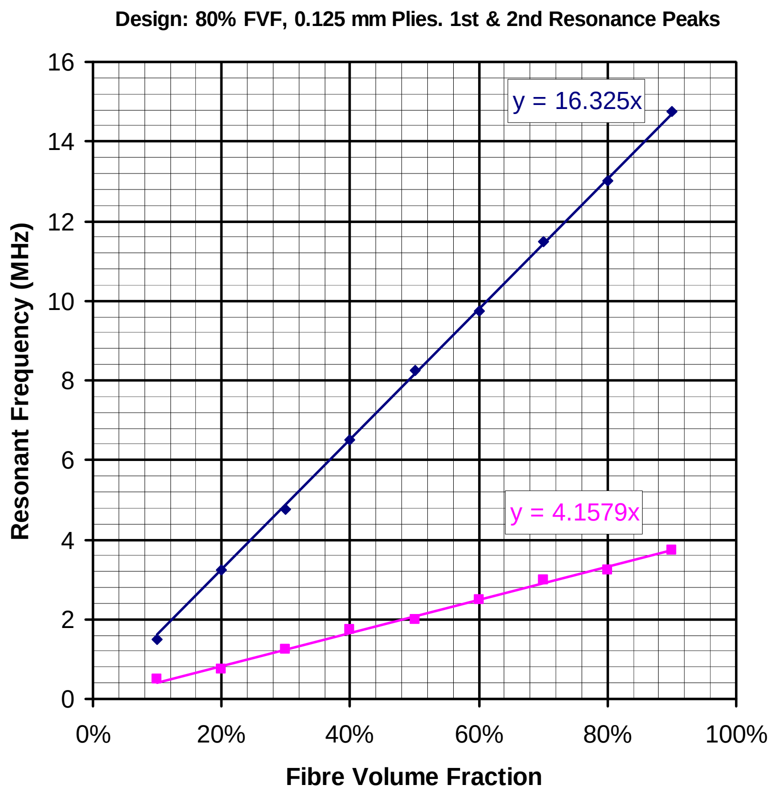

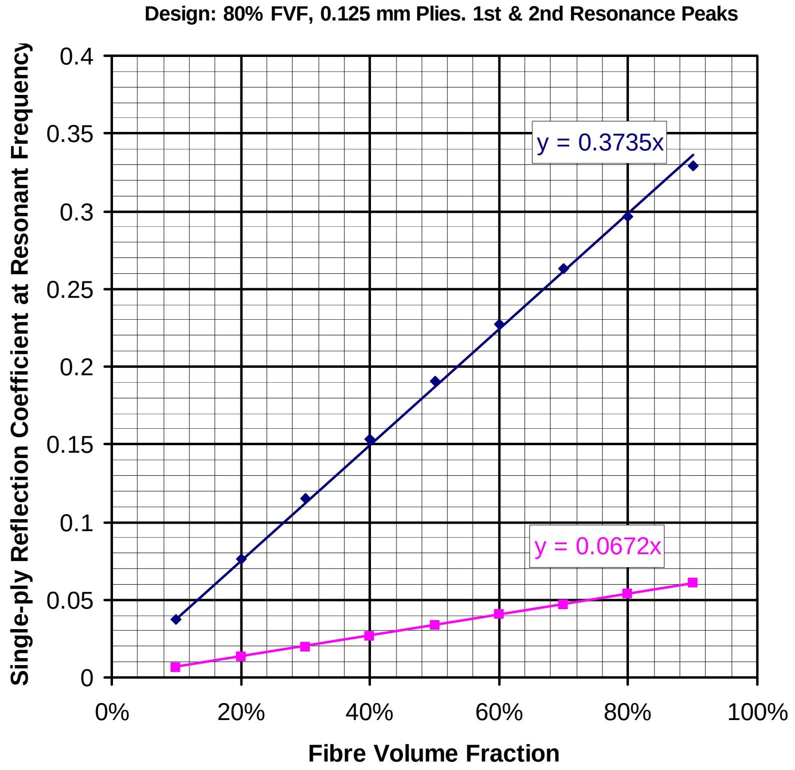

Figure C-4. Graphs of the first (pink) and second (blue) resonant frequencies (top) and the reflection coefficients (bottom) calculated for two interfaces - either side of a single ply – for a range of FVF values for 0.125 mm thick plies (8 plies per millimetre) with a designed 80% volume fraction value.

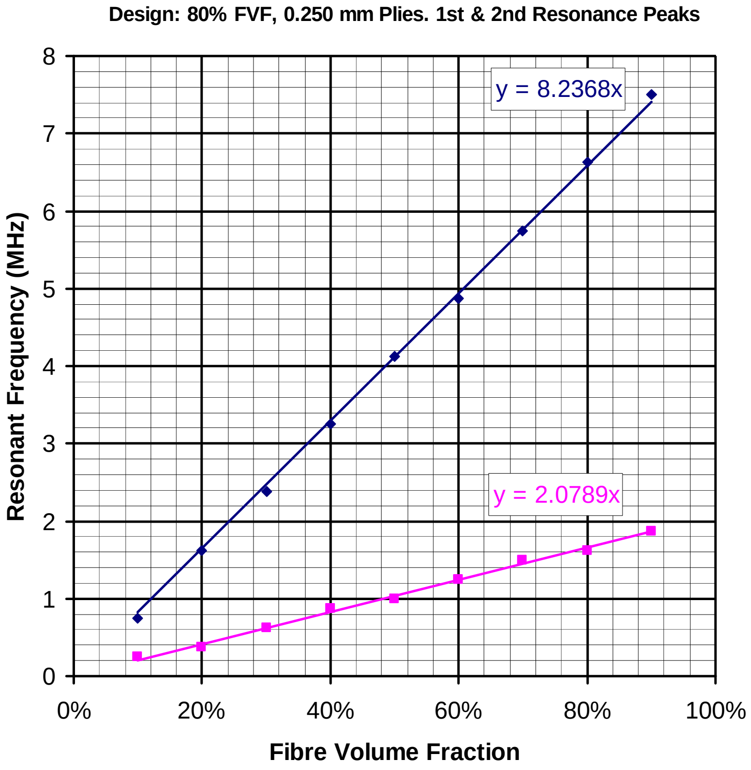

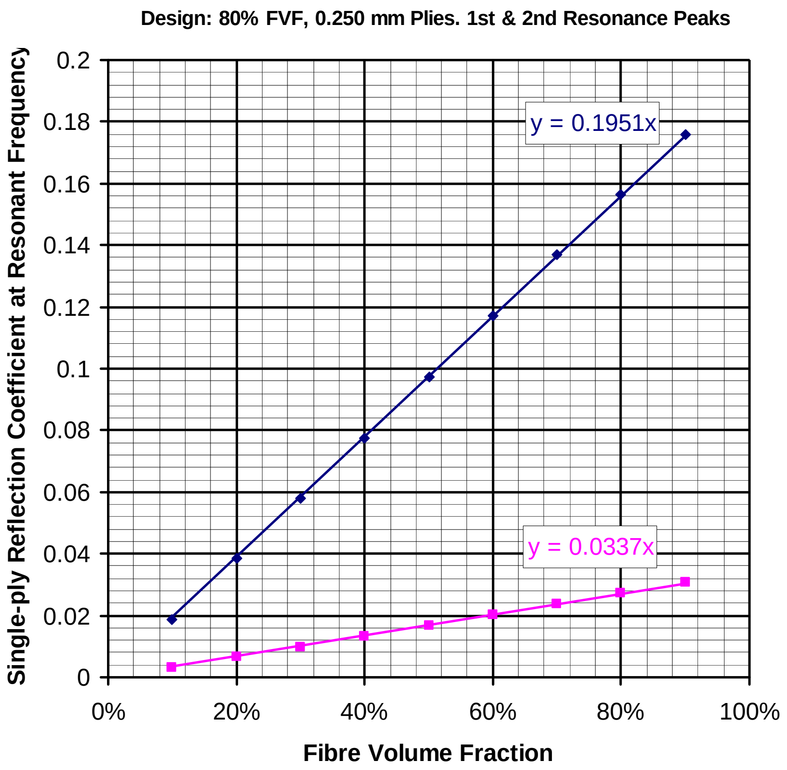

Figure C-5. Graphs of the first (pink) and second (blue) resonant frequencies (top) and the reflection coefficients (bottom) calculated for two interfaces - either side of a single ply – for a range of FVF values for 0.25 mm thick plies (4 plies per millimetre) with a designed 80% volume fraction value.

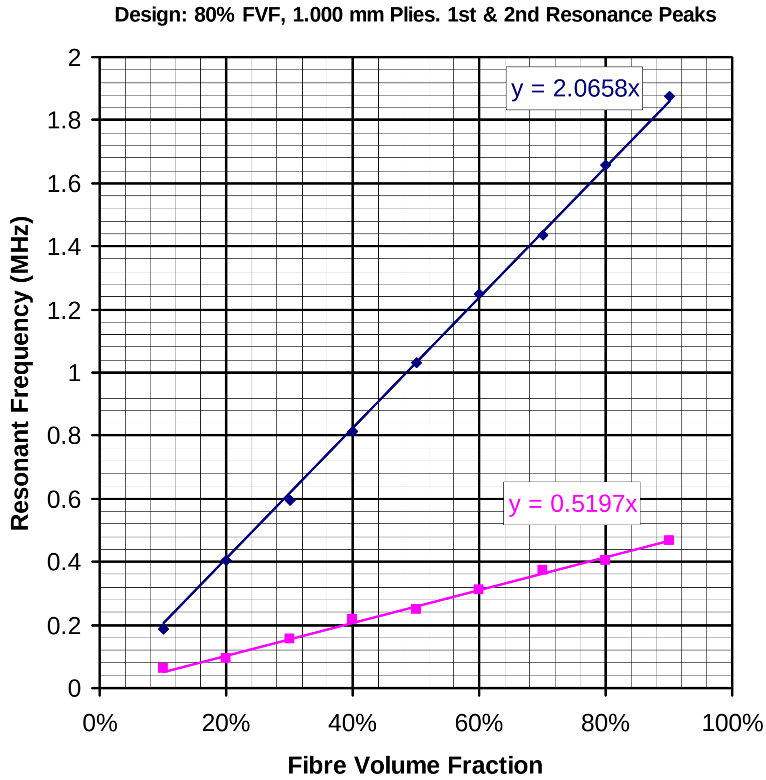

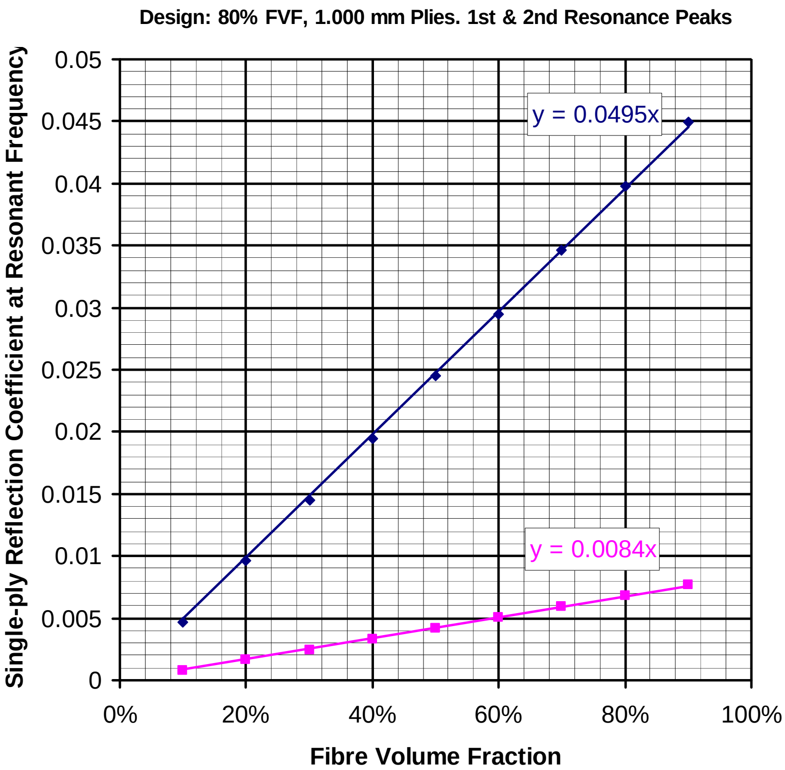

Figure C-6. Graphs of the first (pink) and second (blue) resonant frequencies (top) and the reflection coefficients (bottom) calculated for two interfaces - either side of a single ply – for a range of FVF values for 1.0 mm thick plies (1 ply per millimetre) with a designed 80% volume fraction value.

The graphs in Figure C-7 show that it is possible to calibrate both the resonant frequency and the peak reflection coefficient at resonance against FVF.

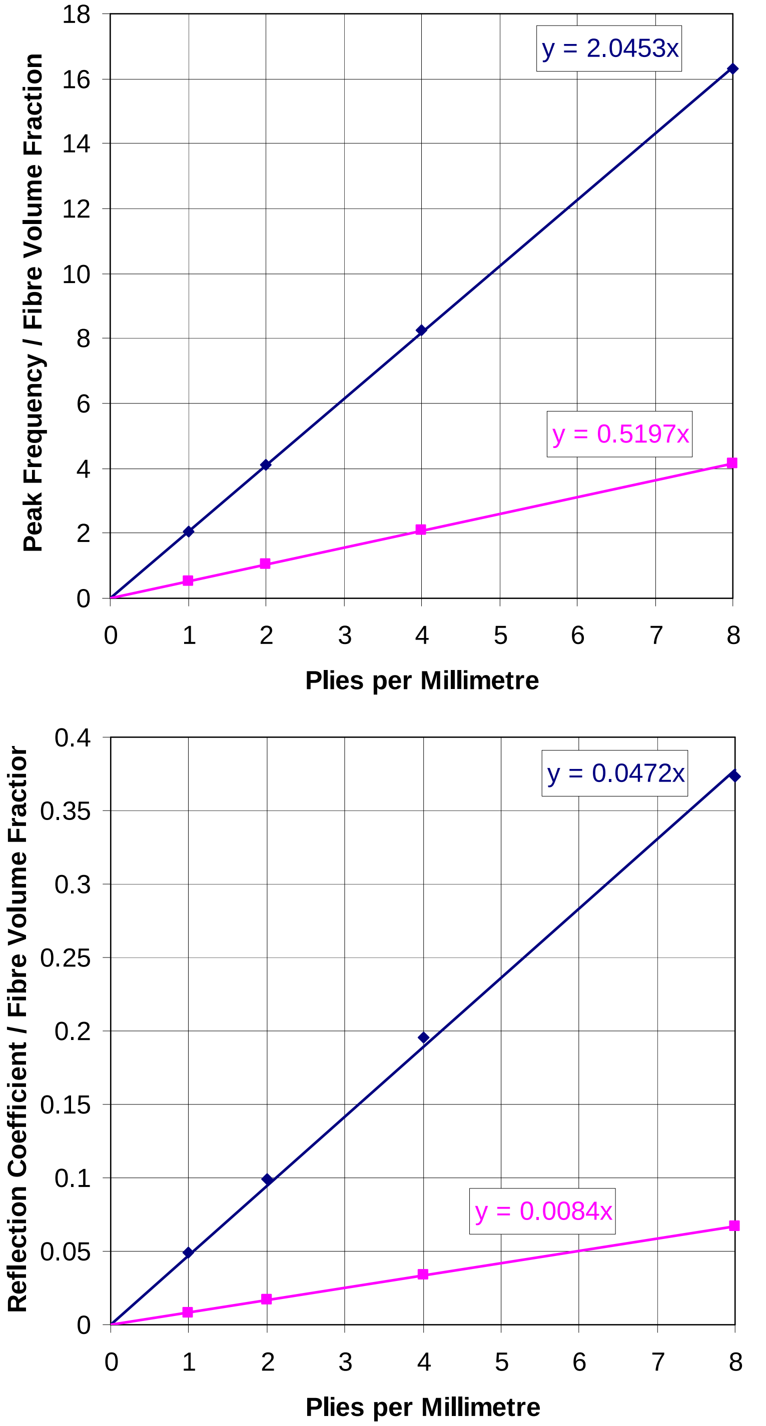

Figure C-7. Calibrations for resonant frequency vs FVF (top) and peak reflection coefficient vs FVF for the first (pink) and second (blue) resonant frequencies as a function of the nominal number of plies per millimetre and for 80% designed FVF in each case.

Figure C-8 shows that the slopes of the graphs in Figure C-7 are dependent on nominal FVF for resonant frequency, but less so for reflection coefficient.

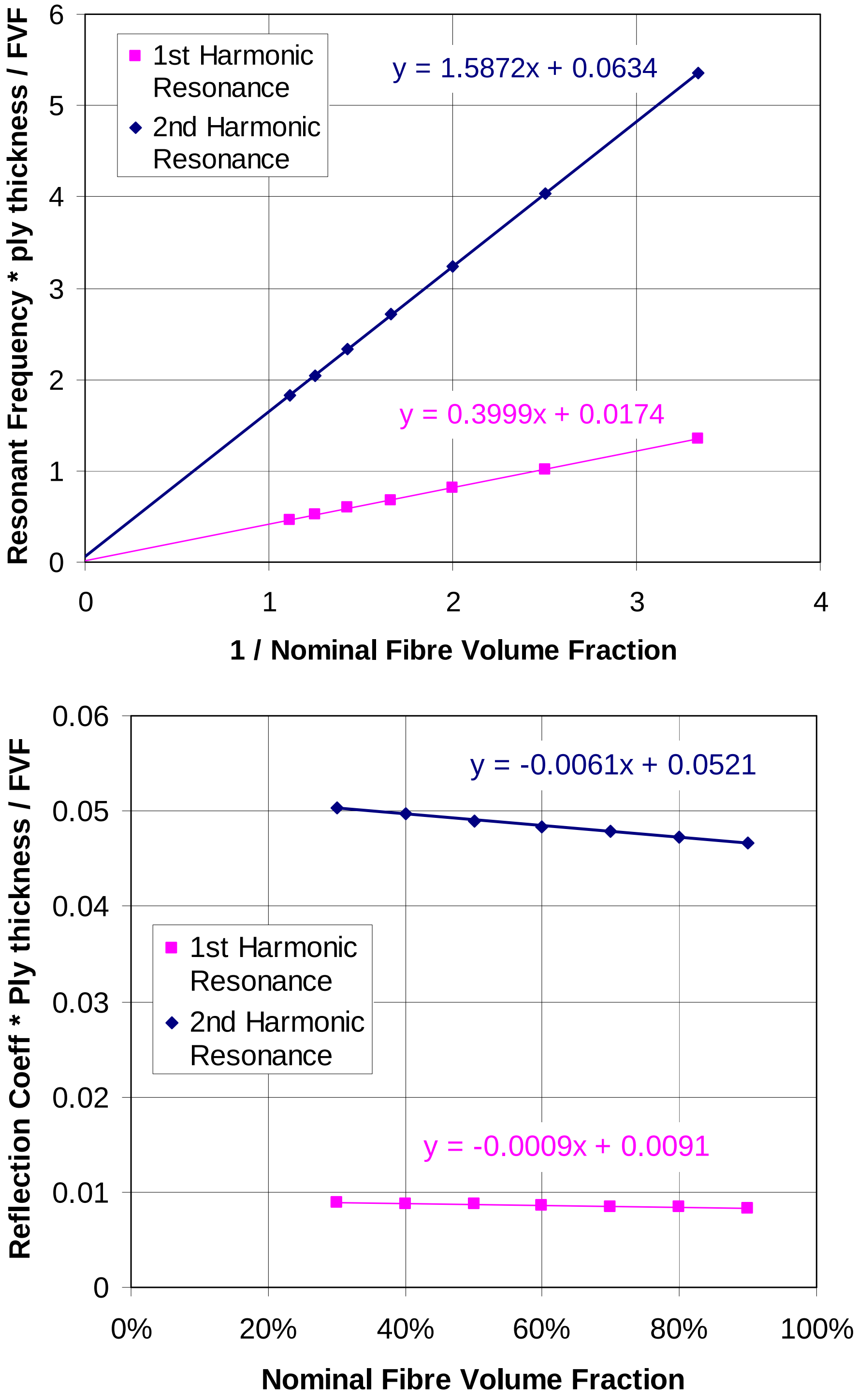

Figure C-8. Graphs showing the variation in slope of the graphs in Figure C-7 with nominal FVF. The top graph plots the resonant frequency dependence and the lower graph plots the reflection coefficient dependence.

Proposed equations for determining FVF have been developed based on the above modelling simulations, which show that a change in the resonance frequency is proportional to the *fractional* change in FVF, but the reflection coefficient at resonance is proportional to absolute FVF. This allows the generation of equations that apply to any composite system provided the nominal ply thickness and nominal FVF are known. The equations are as follows:

$$FVF = \alpha_n f_n t FVF_{nom} \tag{C-1}$$

$$FVF = \beta_n R_n t \tag{C-2}$$

where f_n is the resonance frequency of the nth harmonic resonance, R_n is the corresponding reflection coefficient for the nth harmonic, t is the nominal ply thickness, FVF_{nom} is the nominal FVF and α_n and β_n are the calibration coefficients – note that n=1 for the second resonance. The values for α_n and β_n for the first two resonances (n=0 and n=1) are shown in Figure C-9 and Figure C-10.

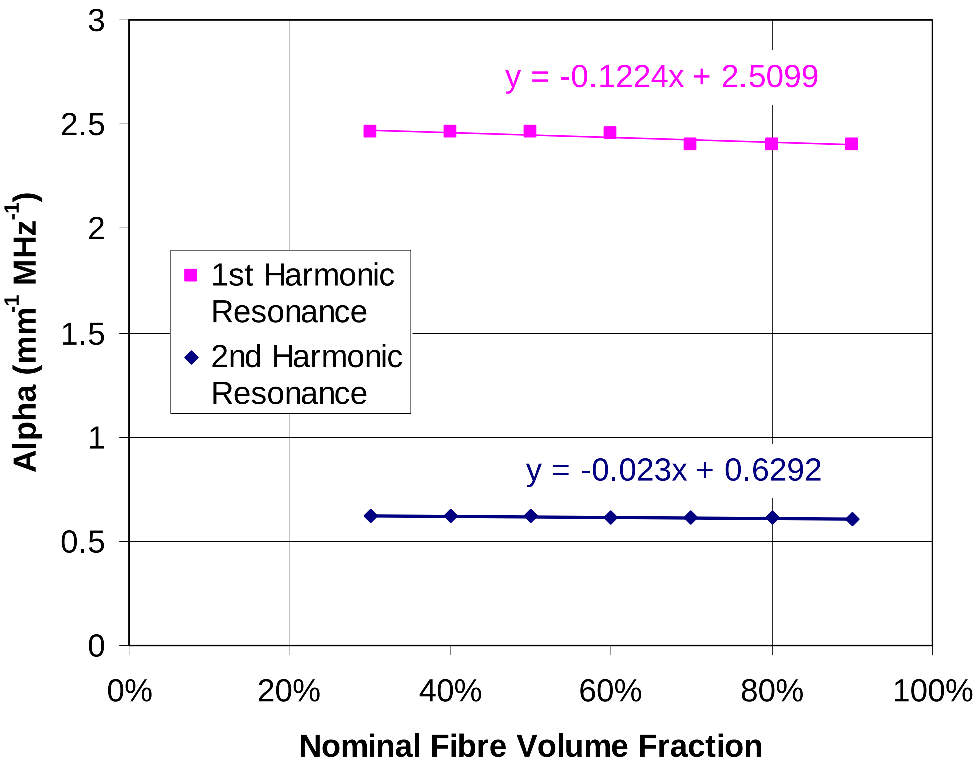

Figure C-9. Variation with nominal FVF of the first two α coefficients for the frequency-based method of measuring FVF using ply resonance effects.

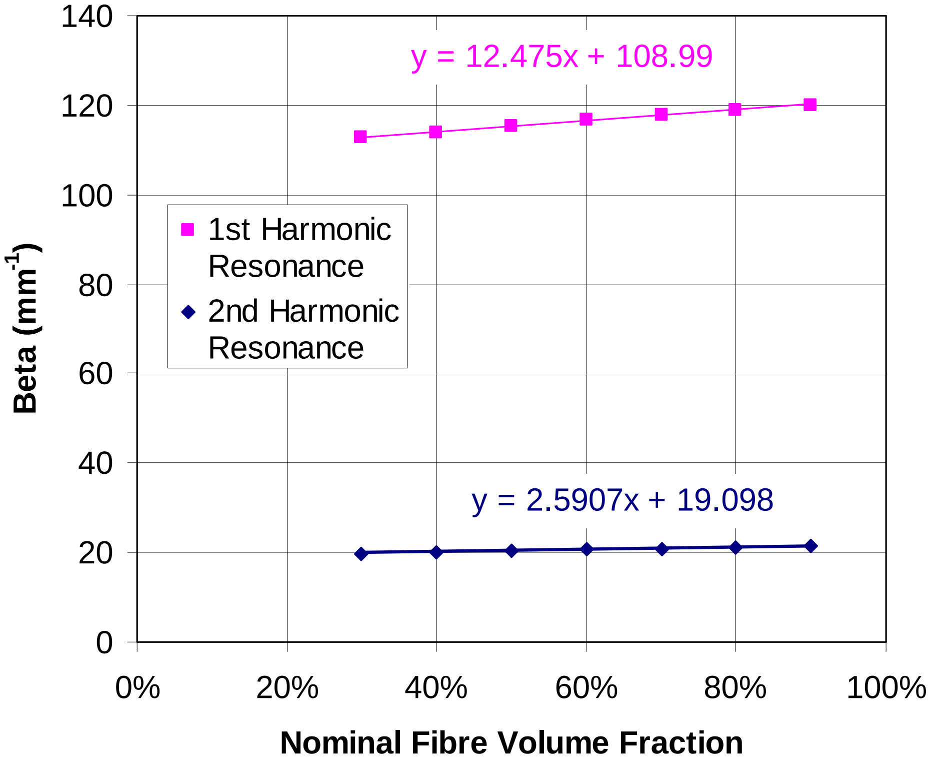

Figure C-10. Variation with nominal FVF of the first two β coefficients for the amplitude-based method of measuring FVF using ply resonance effects.

APPENDIX D Bezier Curves and Hilbert Transforms

D.1 Bezier Curves

Bezier curves (Bartels et al, 1998) are widely used to model smooth curves with just a few control points that can be manipulated by the user in an intuitive way. Quadratic Bezier curves were adequate for this work and are described below

D.1.1 Quadratic Bezier curves

A quadratic Bezier curve touches two lines at specified points on those lines and in each case with a local gradient equal to the gradient of the line it touches. It forms a smooth transition between the two lines. The curve can be defined in terms of just three control points: the point of intersection P_1 of the two lines and the point on each line where the curve just touches, P_0 and P_2.

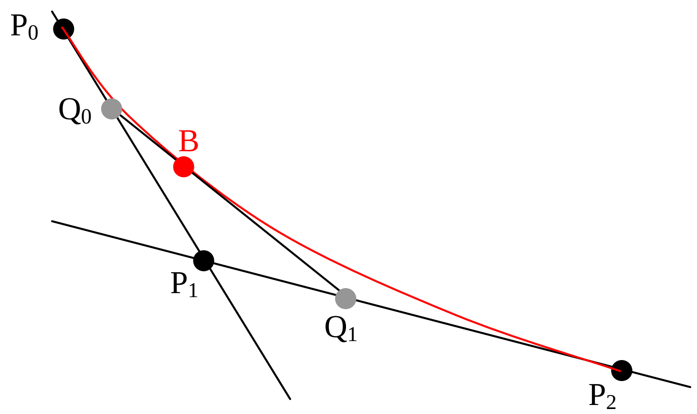

Figure D-1. Construction of a quadratic Bezier curve B using control points P_0, P_1 and P_2.

The principle is that the Bezier curve is the locus of points B such that B is a fraction α along a line between two points Q_0 and Q_1 that are themselves a fraction α along the lines between P_0 and P_1 and P_1 and P_2 respectively. Thus B obeys the following equation which can be used for each of the cartesian coordinates of B, P_0, P_1 and P_2:

$$B(\alpha) = (1-\alpha)P_0 + 2\alpha(1-\alpha)P_1 + \alpha^2 P_2 \qquad \textit{(D-1)}$$

D.2 Hilbert Transforms

D.2.1 Derivation

The Hilbert Transform, named after David Hilbert, was first used as an ultrasonic signal processing tool by Gammell (1981), who described its use to track the reflected energy from a propagation medium. The Hilbert Transform determines from a measured signal the imaginary component of a *complex analytic signal* where the real component is the measured signal. This can be explained as follows.

Gabor (1946) originally defined the *complex analytic signal* as a complex form where the measured signal is just the real component. For example, with a simple harmonic function, the real signal

$$f(t) = a\cos(\omega t) + b\sin(\omega t) \tag{D-2}$$

(where a and b are real constants and ω is the angular frequency) is replaced by the complex form:

$$h(t) = f(t) + ig(t) = (a - ib)\exp(i\omega t) \tag{D-3}$$

The function $g(t)$ is produced from $f(t)$ by replacing cos(ωt) by sin(ωt) and sin(ωt) by -cos(ωt). The function $g(t)$ thus represents a signal in quadrature (retarded by $\pi/2$ radians) with the signal represented by $f(t)$. If $g(t)$ is not a simple harmonic function, the complex analytic signal can be obtained by similar treatment to each Fourier component.

The method of determining the Hilbert Transform in the frequency domain is to *subtract* $\pi/2$ radians from the phase of each frequency component above zero up to the Nyquist frequency (half the sampling frequency) and *add* $\pi/2$ radians to those above the Nyquist frequency (the negative frequency components). However, if the Hilbert Transform is to be combined with the measured signal to form the complex analytic signal, it is multiplied by i, which has the effect of adding $\pi/2$ radians to the phase of all the frequencies, restoring the positive ones and cancelling out the negative ones.

The result is that the complex analytic signal can be created from the original measured signal by just setting all the Fourier components above the Nyquist frequency (the negative frequencies) to zero.

D.2.2 Relationship to power

Heyser (1971) investigated the relationship between the complex analytic signal and the rate of arrival of energy (power). He showed that the square of the magnitude of the complex analytic signal is proportional to the instantaneous rate of arrival of the total energy (ie the power). The square of the real signal, on the other hand, is proportional to the rate of arrival of just one of the components of the energy, such as the kinetic energy, the potential energy, or some linear combination of the two. The square of the real signal could thus be zero at an instant when one of the component energies is zero, whereas the square of the analytic signal magnitude will only be zero when the total (kinetic plus potential) instantaneous energy is zero. Since the analytic signal magnitude is directly related to the rate of energy arrival, it is the optimal estimator of interface location for echo signals of the type commonly used in ultrasound analysis.

D.2.3 Magnitude and phase

As explained above, for a pulse-echo ultrasound inspection, the magnitude of the complex analytic signal represents the instantaneous energy arriving back at the transducer at a given time. The phase of the complex analytic signal indicates the instantaneous proportion of that energy which is in the form of kinetic energy rather than potential energy.

APPENDIX E Focused Ultrasonic Fields

E.1 Terminology

Focusing of a sound beam achieves higher sensitivity and resolution by producing a narrower beam that is more concentrated, and therefore achieves a higher peak acoustic pressure. Even a plane-piston transducer produces a ‘natural focus’ at the last axial maximum (or near-field distance), often represented as N (or Y_0^+). For a circular plane-piston transducer:

$$N = \frac{D^2}{4\lambda} \qquad \text{(E-1)}$$

where D is the transducer’s element diameter and λ is the wavelength.

The ratio of the focal distance z_f to the near-field distance N is known as the focal gain, K_f and this can vary from 0 to 1:

$$K_f = \frac{z_f}{N} \qquad 0 < K_f \leq 1 \qquad \text{(E-2)}$$

Another parameter, familiar from optics, is the F-number – defined as the ratio of focal distance to aperture diameter. In the case of an ultrasonic transducer it can be expressed as follows:

$$F = \frac{z_f}{D} \qquad \text{(E-3)}$$

E.2 Focal beamwidth

There is only an analytical solution for beamwidth at the focus of the transducer. and it is important to distinguish between acoustic-pressure beamwidth in the field and pulse-echo beamwidth. Figure E-1 and the following equations describe the -6 dB beamwidth for acoustic pressure in the field (Krautkramer and Krautkramer, 1969) and in pulse-echo mode (ASM Handbook).

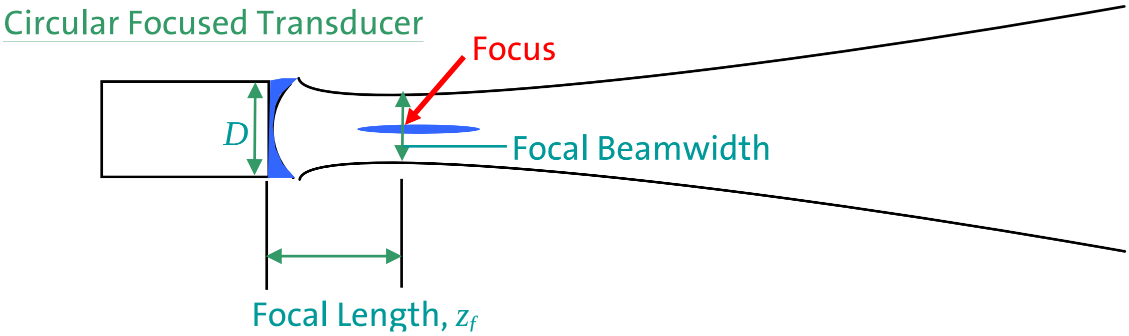

Figure E-1. Diagram showing the parameters used to calculate focal beamwidth.

Acoustic Pressure in the field: -6 dB Focal Beamwidth = 1.396 $\lambda z_f / D$

Pulse-echo response: -6 dB Focal Beamwidth = 1.032 $\lambda z_f / D$

E.3 Axial profile

According to O'Neil (1949) the on-axis acoustic pressure p is given by:

$$p = p_0 \left| \frac{2}{1 - \frac{z}{r}} \right| \left| \sin\left[\frac{\pi}{\lambda} \left(\sqrt{(z-h)^2 + \frac{D^2}{4}} - z \right) \right] \right| \qquad \text{(E-4)}$$

where z is the distance on the axis from the transducer element, r is the radius of curvature of the spherically-curved element surface and h is given by:

$$h = r - \sqrt{r^2 - \frac{D^2}{4}} \qquad \text{(E-5)}$$

An example of the axial profile is given in Figure E-2 and Figure E-3 for 5 MHz and 10 MHz transducers respectively of diameter 12.7 mm and radius of curvature 75 mm

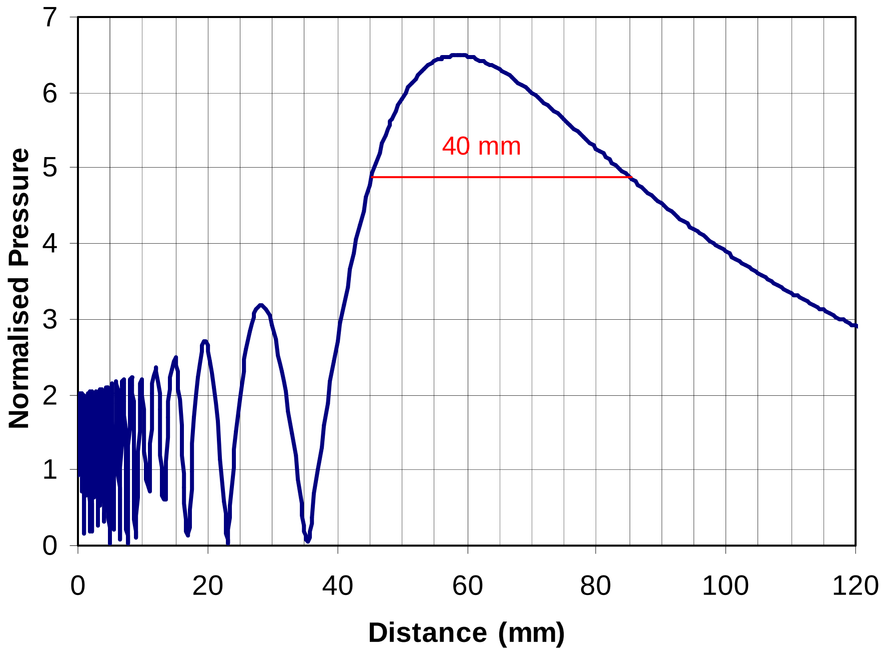

Figure E-2. Normalised on-axis acoustic pressure p/p_0 (where p_0 is pressure at the transducer) as a function of distance in water for a 12.7 mm (0.5") diameter 5 MHz transducer with radius of curvature 75 mm. The -3 dB Pressure Focal Range, shown in red, corresponds to the -6 dB Pulse-Echo Focal Range.

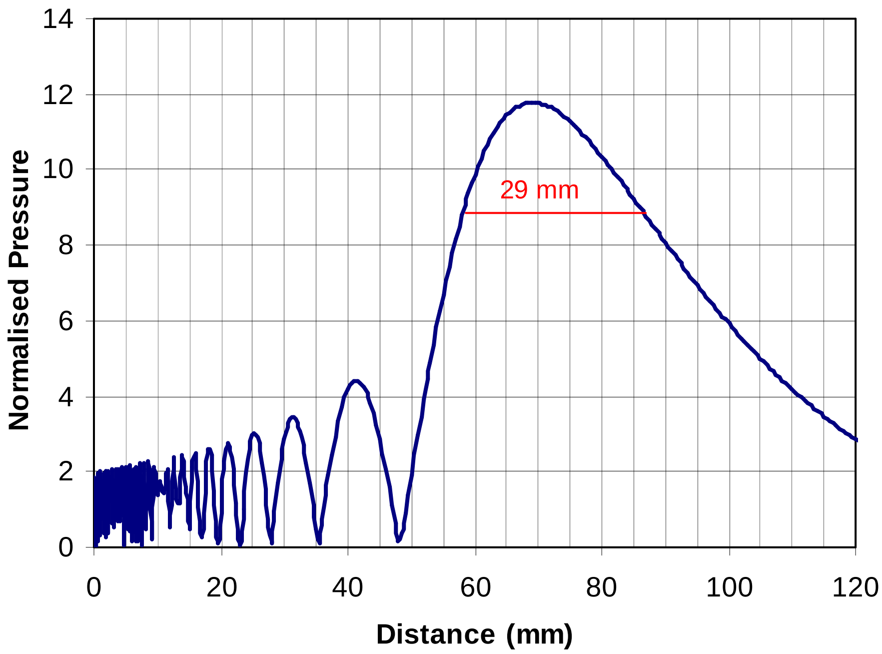

Figure E-3. Normalised on-axis acoustic pressure p/p_0 (where p_0 is pressure at the transducer) as a function of distance in water for a 12.7 mm (0.5") diameter 10 MHz transducer with radius of curvature 75 mm. The -3 dB Pressure Focal Range, shown in red, corresponds to the -6 dB Pulse-Echo Focal Range.

E.4 -6 dB Pulse-Echo Focal Range

The -6 dB Pulse-Echo Focal Range can be defined as the distance between the -6 dB threshold axial points measuring the pulse-echo response from a point reflector. This is equivalent to using a -3 dB threshold with a measurement of acoustic pressure as in Figure E-3 because diffraction effects will be applied on both the transmission and reception stages.

Ideally it would be possible to obtain an analytical expression for this -3 dB acoustic pressure focal range from Equation E-4. However, when this was attempted using Mathematica it was found not to be possible. Instead, the -3 dB points were determined numerically for a range of focal gains (K_f) and these were used to determine the -6 dB Pulse-Echo Focal Range, z_r. The values, normalised to the near-field distance, N, are plotted in Figure E-4 for 5MHz and Figure E-5 for 10 MHz. A polynomial fit to these values suggests that a quadratic relationship with focal gain is appropriate.

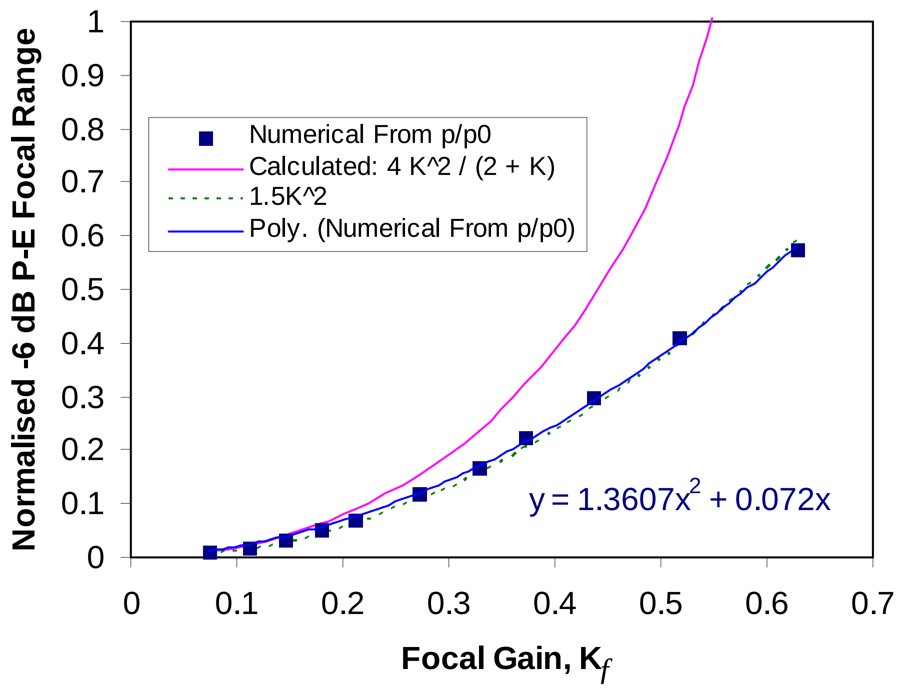

Figure E-4. -6 dB Pulse-Echo Focal Range determined numerically (squares) from the -3 dB acoustic pressure focal range from Equation E-4. 5 MHz transducers of diameter 12.7 mm (0.5”) were simulated with different radii of curvature. The relationships given in Equations E-7 and E-8 are also shown.

The quadratic relationship suggested from Figure E-4 is:

$$z_r = NK_f(1.36K_f + 0.072) \qquad \textit{(E-6)}$$

For focal gains in the range plotted, the dashed curves in Figure E-4 and Figure E-5 show that the relationship can be approximated to:

$$z_r \approx 1.5NK_f^2 \qquad \textit{(E-7)}$$

Another relationship (Equation E-8) has been given in a Panametrics transducer technical note (Panametrics 1993) but no source was quoted. This relationship is also shown in Figure E-4 and Figure E-5:

$$z_r = NK_f^2\left(\frac{4}{K_f + 2}\right) \qquad \textit{(E-8)}$$

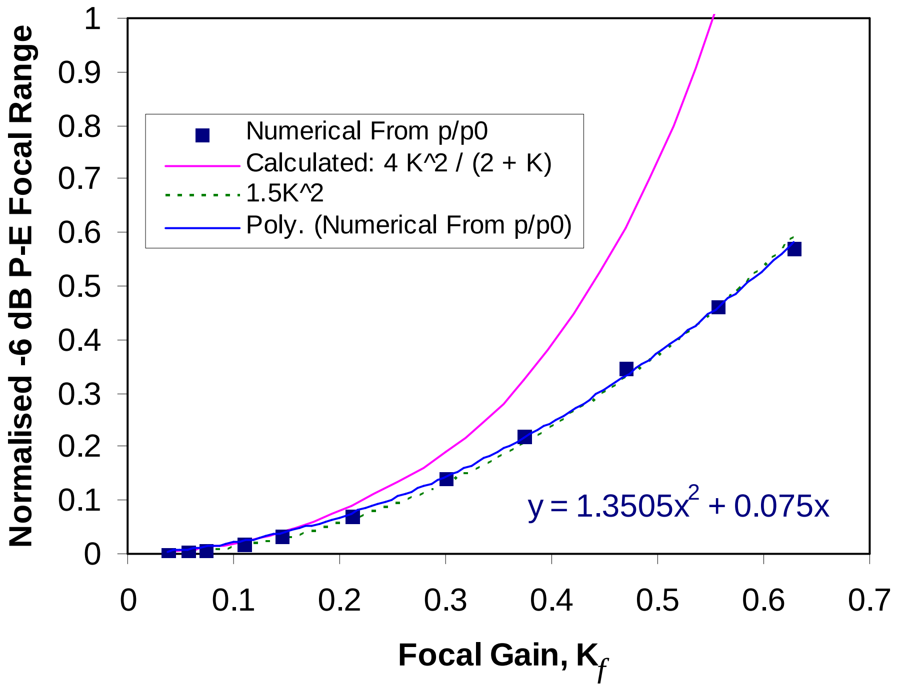

Figure E-5. -6 dB Pulse-Echo Focal Range determined numerically (squares) from the -3 dB acoustic pressure focal range from Equation E-4. 10 MHz transducers of diameter 12.7 mm (0.5") were simulated with different radii of curvature. The relationships given in Equations E-7 and E-8 are also shown.

APPENDIX F Equivalent Media Modelling

F.1 Introduction

After starting the literature review of equivalent media modelling methods, two issues became evident. Firstly, most of the literature dated back to the 1960s and 1970s with little work following that, suggesting either that the problems had been solved, or that the need for better models disappeared. Secondly, several of the key papers were poorly written and/or contained mistakes in important equations. For the purposes of this project and future work in this area, There was a need for a careful analysis of the literature, identification of mistakes and a recommendation for the best models for predicting transverse compression modulus and transverse shear modulus in both carbon and glass fibre composites.

This appendix reports a detailed study of the models and includes comparisons of predictions for carbon-fibre and glass-fibre composite materials, and for porosity in carbon-fibre composite. It begins with definitions of symbols and a self-consistent terminology.

F.2 Nomenclature

The following definitions of symbols will be used in this appendix

E	Young's modulus
G, G_v, G_f	Shear modulus, shear modulus of voids (air), and of fibre
K, K_v, K_f	Bulk modulus, bulk modulus of voids (air), bulk modulus of fibre.
M	Compression modulus
C_{ij}	Stiffness matrix
ν	Poisson's ratio
ε_j	Strain tensor
ϕ_f, ϕ_m, ϕ_v	Fibre, matrix, and void volume fraction respectively
ρ	Density
σ_i	Stress tensor

F.3 Elastic Moduli

F.3.1 Moduli in isotropic materials

The definitions of the four elastic moduli: bulk modulus, shear modulus, Young's modulus and longitudinal (compression) modulus are defined for isotropic materials as follows.

Bulk modulus

The **bulk modulus**, K measures a materials resistance to uniform compression. It is defined as the pressure increase needed to cause a given relative decrease in volume and can be formally defined by the following equation:

$$K = -V \frac{\partial p}{\partial V} \tag{F-1}$$

where p is pressure and V is volume (see Figure F-1).

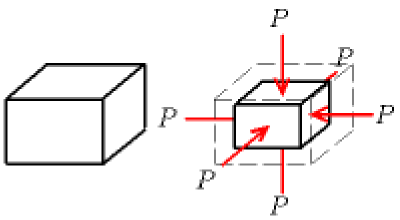

Figure F-1. Diagram illustrating uniform pressure applied to a solid material.

Bulk modulus is related to shear modulus K and Young's modulus E via Poisson's ratio, ν as follows:

$$K = \frac{2G(1+\nu)}{3(1-2\nu)}$$
$$K = \frac{E}{3(1-2\nu)} \tag{F-2}$$

Shear modulus

The **shear modulus** (or modulus of rigidity) G is a measure of a material's response to a shearing stress and is defined as the ratio of shear stress to shear strain, or formally by the following equation:

$$G = \frac{\sigma_{xy}}{\varepsilon_{xy}} = \frac{F/A}{\Delta x / I} = \frac{FI}{\Delta x A} \quad \textit{(F-3)}$$

where $\sigma_{xy}=F/A$ is the shear stress in the x-y plane, $\varepsilon_{xy}=\Delta x/I$ is the shear strain in the x-y plane, F is the force, A is the area over which the force acts, I is the distance between the two opposing forces and Δx is the transverse displacement (see Figure F-2).

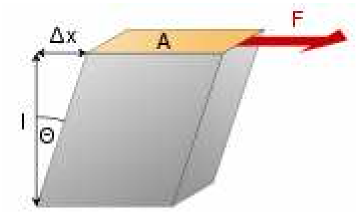

Figure F-2. Diagram explaining the parameters used in the definition of shear modulus.

Shear modulus is related to bulk modulus and Young's modulus via Poisson's ratio, ν as follows:

$$G = \frac{3K(1-2\nu)}{2(1+\nu)}$$
$$G = \frac{E}{2(1+\nu)} \quad \textit{(F-4)}$$

Young's modulus

The **Young's modulus** E describes a material's resistance to a uniaxial linear stress when not clamped laterally and is defined as the ratio of uniaxial stress to uniaxial strain in the range of stress in which Hooke's law holds (the elastic range), or more formally as:

$$E = \frac{\sigma_{xx}}{\varepsilon_{xx}} = \frac{F/A}{\Delta l/L} = \frac{FL}{\Delta l A} \qquad \text{(F-5)}$$

where $\sigma_{xx}=F/A$ is the uniaxial stress in the x direction, $\varepsilon_{xx}=\Delta l/L$ is the shear strain in the x direction, F is the force, A is the area over which the force acts, L is the original length and Δl is the uniaxial displacement (see Figure F-3).

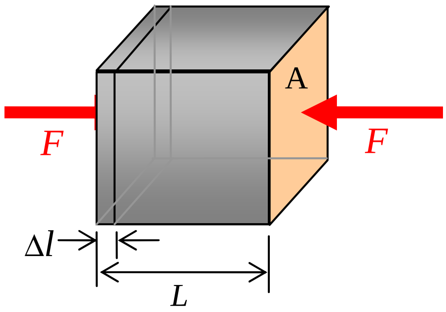

Figure F-3. Diagram illustrating the parameters used in the definition of Young's modulus.

Young's modulus is related to bulk modulus and shear modulus via Poisson's ratio, ν as follows:

$$\begin{aligned} E &= 3K(1-2\nu) \\ E &= 2G(1+\nu) \end{aligned} \qquad \text{(F-6)}$$

Longitudinal (compression) modulus

The **Longitudinal (compression) modulus** M is of great interest for ultrasonic propagation studies where longitudinal-wave propagation is involved. It is defined as the ratio of uniaxial stress to uniaxial strain when all strains in other directions are zero. It can be shown that:

$$M = \rho c^2 \qquad \text{(F-7)}$$

where c is the sound speed of a longitudinal wave and ρ is the density of the material. The longitudinal modulus is related to the other moduli as follows:

$$
\begin{aligned}
M &= K + \tfrac{4}{3}G \\
M &= E\frac{1-\nu}{(1+\nu)(1-2\nu)} \\
M &= 3K\frac{1-\nu}{1+\nu} \\
M &= 2G\frac{1-\nu}{1-2\nu}
\end{aligned}
\qquad \text{(F-8)}
$$

F.3.2 Moduli in anisotropic materials

In anisotropic materials, **Young's modulus** is not the same in all directions. Usually a suffix is used to indicate the direction in which the stress has been applied and strain measured.

For crystalline solids with a symmetry lower than cubic the **bulk modulus** is not the same in all directions and needs to be described with a tensor with more than one independent value. However, it is possible to define a **plane strain bulk modulus** which is useful when a component is long in one direction and so strain in that direction is limited by surrounding material, allowing strain only in the cross-sectional plane.

Shear modulus is defined in a plane containing the stress vectors that cause the shear effect. In anisotropic materials this plane is usually specified as a suffix.

The elastic moduli appropriate to different symmetry types of anisotropic materials will be discussed below.

F.4 Elastic stiffness matrices

F.4.1 Stress analysis

The state of stress at a point in a body can be defined by all the stress vectors $\boldsymbol{T}^{(n)}$ associated with all n planes (infinite number of planes) that pass through that point. But, according to *Cauchy's fundamental theorem*, by just knowing the stress vectors on three orthogonal planes, the stress vector on any other plane passing through that point can be found through coordinate transformation equations. Assuming a material element exists (Figure F-4) with element planes perpendicular to the cartesian coordinate axes and having normal vectors $\boldsymbol{e_1}$, $\boldsymbol{e_2}$ and $\boldsymbol{e_3}$, the stress vectors associated with each of the element planes, i.e. $\boldsymbol{T^{(e1)}}$, $\boldsymbol{T^{(e2)}}$, $\boldsymbol{T^{(e3)}}$ can be decomposed into components in the direction of the three coordinate axes as follows:

$$\begin{aligned} T^{(e_1)} &= \sigma_{11}e_1 + \sigma_{12}e_2 + \sigma_{13}e_3 \\ T^{(e_2)} &= \sigma_{21}e_1 + \sigma_{22}e_2 + \sigma_{23}e_3 \\ T^{(e_3)} &= \sigma_{31}e_1 + \sigma_{32}e_2 + \sigma_{33}e_3 \end{aligned} \qquad \text{(F-9)}$$

or, in index notation:

$$T^{(e_i)} = \sigma_{ij}e_j \qquad \text{(F-10)}$$

where σ_{11}, σ_{22} and σ_{33} are normal stresses whilst $\sigma_{12}, \sigma_{13}, \sigma_{21}, \sigma_{23}, \sigma_{31}$ and σ_{32} are shear stresses.

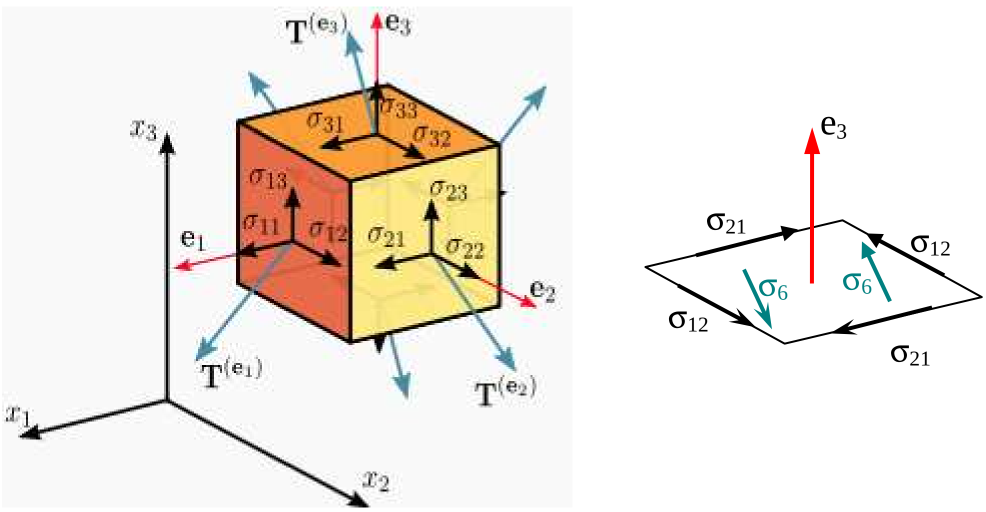

Figure F-4. Diagram of generalised stress vectors acting at a point (left) and just the shear stresses acting in a plane perpendicular to the 3 direction (right) which can be represented by index 6 in the Voigt notation.

The first index i indicates that the stress acts on a plane normal to the x_i axis, and the second index j denotes the direction in which the stress acts.

The Voigt notation representation of the stress tensor takes advantage of the symmetry of the stress tensor to express the stress as a 6-dimensional vector of the form σ_i where indices 1, 2 and 3 represent normal plane stresses in the three orthogonal directions and indices 4, 5 and 6 represent shear stresses in planes normal to directions 1, 2 and 3 respectively (see Figure F-4-right)

$$\begin{bmatrix} \sigma_1 \\ \sigma_2 \\ \sigma_3 \\ \sigma_4 \\ \sigma_5 \\ \sigma_6 \end{bmatrix} \equiv \begin{bmatrix} \sigma_{11} \\ \sigma_{22} \\ \sigma_{33} \\ \sigma_{23,32} \\ \sigma_{31,13} \\ \sigma_{12,21} \end{bmatrix} \qquad \textit{(F-11)}$$

For the purposes of this analysis, fibres will be assumed to be placed in the '3' direction, although some authors use the '1' direction for fibres (see Figure F-5).

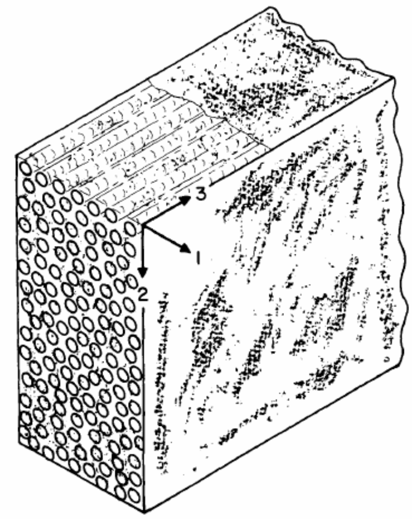

$$\begin{bmatrix} C_{11} & C_{12} & C_{13} & C_{14} & C_{15} & C_{16} \\ C_{12} & C_{22} & C_{23} & C_{24} & C_{25} & C_{26} \\ C_{13} & C_{23} & C_{33} & C_{34} & C_{35} & C_{36} \\ C_{14} & C_{24} & C_{34} & C_{44} & C_{45} & C_{46} \\ C_{15} & C_{25} & C_{35} & C_{45} & C_{55} & C_{56} \\ C_{16} & C_{26} & C_{36} & C_{46} & C_{56} & C_{66} \end{bmatrix}$$

Figure F-5. Diagram (from R E Smith, 1972) showing the Cartesian axes relative to the fibre direction in a fibre composite and the general stiffness matrix for anisotropic materials.

Also in Figure F-5 is the generic stiffness matrix C_{ij} relating the strain tensor ε_j to the stress tensor σ_i in anisotropic materials, as follows.

$$
\begin{bmatrix} \sigma_1 \\ \sigma_2 \\ \sigma_3 \\ \sigma_4 \\ \sigma_5 \\ \sigma_6 \end{bmatrix} = \begin{bmatrix} C_{11} & C_{12} & C_{13} & C_{14} & C_{15} & C_{16} \\ C_{12} & C_{22} & C_{23} & C_{24} & C_{25} & C_{26} \\ C_{13} & C_{23} & C_{33} & C_{34} & C_{35} & C_{36} \\ C_{14} & C_{24} & C_{34} & C_{44} & C_{45} & C_{46} \\ C_{15} & C_{25} & C_{35} & C_{45} & C_{55} & C_{56} \\ C_{16} & C_{26} & C_{36} & C_{46} & C_{56} & C_{66} \end{bmatrix} \begin{bmatrix} \varepsilon_1 \\ \varepsilon_2 \\ \varepsilon_3 \\ \varepsilon_4 \\ \varepsilon_5 \\ \varepsilon_6 \end{bmatrix} \quad \textit{(F-12)}
$$

Accepted terminology is that suffixes 1, 2 and 3 are three orthogonal plane strain directions in 3D space, and 4, 5 and 6 are shear strains in planes perpendicular to directions 1, 2 and 3 respectively.

F.4.2 Isotropic materials

For isotropic materials, where the properties are independent of the orientation of the material, the stiffness matrix can be reduced to just two independent elements: the bulk modulus K and the shear modulus G, as follows:

$$
\begin{bmatrix} \sigma_1 \\ \sigma_2 \\ \sigma_3 \\ \sigma_4 \\ \sigma_5 \\ \sigma_6 \end{bmatrix} = \begin{bmatrix} K+\frac{4}{3}G & K-\frac{2}{3}G & K-\frac{2}{3}G & 0 & 0 & 0 \\ K-\frac{2}{3}G & K+\frac{4}{3}G & K-\frac{2}{3}G & 0 & 0 & 0 \\ K-\frac{2}{3}G & K-\frac{2}{3}G & K+\frac{4}{3}G & 0 & 0 & 0 \\ 0 & 0 & 0 & G & 0 & 0 \\ 0 & 0 & 0 & 0 & G & 0 \\ 0 & 0 & 0 & 0 & 0 & G \end{bmatrix} \begin{bmatrix} \varepsilon_1 \\ \varepsilon_2 \\ \varepsilon_3 \\ \varepsilon_4 \\ \varepsilon_5 \\ \varepsilon_6 \end{bmatrix} \quad \text{(F-13)}
$$

Note that the diagonal moduli for normal plane stresses and strains are equal to the longitudinal modulus, $M = K + \frac{4}{3}G$.

F.4.3 Anisotropic materials

Orthotropic materials

For Orthotropic materials (which have three orthogonal planes of symmetry) the stiffness matrix can be reduced to the following:

$$\begin{bmatrix}\sigma_1\\\sigma_2\\\sigma_3\\\sigma_4\\\sigma_5\\\sigma_6\end{bmatrix}=\begin{bmatrix}C_{11} & C_{12} & C_{13} & 0 & 0 & 0\\ C_{12} & C_{22} & C_{23} & 0 & 0 & 0\\ C_{13} & C_{23} & C_{33} & 0 & 0 & 0\\ 0 & 0 & 0 & C_{44} & 0 & 0\\ 0 & 0 & 0 & 0 & C_{55} & 0\\ 0 & 0 & 0 & 0 & 0 & C_{66}\end{bmatrix}\begin{bmatrix}\varepsilon_1\\\varepsilon_2\\\varepsilon_3\\\varepsilon_4\\\varepsilon_5\\\varepsilon_6\end{bmatrix} \qquad \textit{(F-14)}$$

Cubic symmetrical materials

In the simple case of cubic symmetry, the matrix reduces to the following:

$$\begin{bmatrix}\sigma_1\\\sigma_2\\\sigma_3\\\sigma_4\\\sigma_5\\\sigma_6\end{bmatrix}=\begin{bmatrix}C_{11} & C_{12} & C_{12} & 0 & 0 & 0\\ C_{12} & C_{11} & C_{12} & 0 & 0 & 0\\ C_{12} & C_{12} & C_{11} & 0 & 0 & 0\\ 0 & 0 & 0 & C_{44} & 0 & 0\\ 0 & 0 & 0 & 0 & C_{44} & 0\\ 0 & 0 & 0 & 0 & 0 & C_{44}\end{bmatrix}\begin{bmatrix}\varepsilon_1\\\varepsilon_2\\\varepsilon_3\\\varepsilon_4\\\varepsilon_5\\\varepsilon_6\end{bmatrix} \qquad \textit{(F-15)}$$

which contains just three independent stiffness constants: C_{11}, C_{12} and C_{44}.

Kantor and Bergman (1982) define three elastic moduli in terms of these stiffness constants:

$$\begin{aligned}K &= \tfrac{1}{4}(C_{11}+C_{22}+2C_{12})\\ G_1 &= C_{44}\\ G_2 &= \tfrac{1}{4}(C_{11}+C_{22}-2C_{12})\end{aligned} \qquad \textit{(F-16)}$$

Transversely isotropic materials

For a transversely isotropic material (where the material is symmetric about an axis of rotation, such as the axis of a fibre) with an axis of symmetry in the 3 direction, the stiffness matrix reduces to the following:

$$\begin{bmatrix}\sigma_1\\\sigma_2\\\sigma_3\\\sigma_4\\\sigma_5\\\sigma_6\end{bmatrix}=\begin{bmatrix}C_{11} & C_{12} & C_{13} & 0 & 0 & 0\\ C_{12} & C_{11} & C_{13} & 0 & 0 & 0\\ C_{13} & C_{13} & C_{33} & 0 & 0 & 0\\ 0 & 0 & 0 & C_{44} & 0 & 0\\ 0 & 0 & 0 & 0 & C_{44} & 0\\ 0 & 0 & 0 & 0 & 0 & \tfrac{1}{2}(C_{11}-C_{12})\end{bmatrix}\begin{bmatrix}\varepsilon_1\\\varepsilon_2\\\varepsilon_3\\\varepsilon_4\\\varepsilon_5\\\varepsilon_6\end{bmatrix} \qquad \textit{(F-17)}$$

containing just five independent stiffness constants: C_{11}, C_{12}, C_{13}, C_{33} and C_{44}.

Plane strain bulk modulus is useful in transversely isotropic materials when a component is long in one direction. This is the kind of modulus that is used by several of the models below for fibres in composite, where the plane-strain bulk modulus transverse to the axis can be called the **transverse bulk modulus** K_T and has been quoted by Torquato and Lado (1992) as follows:

$$K_T = K + \tfrac{1}{3}G \tag{F-18}$$

Shear modulus is defined in a plane containing the stress vectors that cause the shearing effect. In transversely isotropic materials this plane can either be perpendicular (transverse) or parallel (axial) to the axis, resulting in two shear moduli: **transverse shear modulus** G_T, and **axial shear modulus** G_A.

F.5 Ultrasonic Velocity

F.5.1 Longitudinal Velocity

Perpendicular to the fibres, the compression-wave velocity c_L is given by Martin (1976) as:

$$c_L = \sqrt{\frac{C_{22}}{\rho}} \tag{F-19}$$

F.5.2 Shear Velocity

For shear waves with a polarisation perpendicular to the fibres (in the 3 direction), the shear-wave velocity c_S is given by Martin (1976) as:

$$c_S = \sqrt{\frac{C_{22} - C_{23}}{2\rho}} \tag{F-20}$$

although Martin also states this for anisotropic fibres but changes C_{23} to C_{12}.

F.6 Spherical isotropic inclusions

F.6.1 Hashin (1962) mixture rule

Hashin (1962) is the definitive work on spherical isotropic inclusions in an isotropic medium. Hashin considered the change in strain energy in a loaded homogeneous body due to the insertion of inhomogeneities. Two geometrical assumptions were made: 1) that the inclusions are spherical and 2) that the action on any one inclusion is transmitted through a spherical shell existing wholly in the surrounding matrix. He generated upper and lower bounds for both bulk and shear modulus of the mixture. For bulk modulus, K^* these coincide to give a single equation (Equation F-21), but not for shear modulus, G^*. Hashin offers an equation for shear modulus (Equation F-22) that always falls between the upper and lower bounds and suggests that when the difference between moduli of the two phases is small then this is a good approximation to the shear modulus.

$$\frac{K^*}{K_m} = 1 + \frac{3(1-\nu_m)\left(\frac{K_v}{K_m} - 1\right)\phi_v}{2(1-2\nu_m) + (1+\nu_m)\left[\frac{K_v}{K_m} - \left(\frac{K_v}{K_m} - 1\right)\phi_v\right]} \tag{F-21}$$

$$\frac{G^*}{G_m} = 1 + \frac{15(1-\nu_m)\left(\frac{G_v}{G_m} - 1\right)\phi_v}{7 - 5\nu_m + 2(4-5\nu_m)\left[\frac{G_v}{G_m} - \left(\frac{G_v}{G_m} - 1\right)\phi_v\right]} \tag{F-22}$$

where ϕ_v is the void volume fraction of porosity, ν_m is the Poisson's ratio for the matrix, K_m and K_v are the bulk moduli for the matrix and voids respectively, and G_m and G_v are the shear moduli for the matrix and voids respectively.

Then Hashin derives terms for the bulk (K^*) and shear (G^*) moduli in the very small concentration limit, which are given in Equations F-23 and F-24):

$$\frac{K^*}{K_m} = 1 - \frac{3(1-\upsilon_m)\left(1-\frac{K_v}{K_m}\right)}{2(1-2\upsilon_m)+(1+\upsilon_m)\frac{K_v}{K_m}}\phi_v \qquad \textit{(F-23)}$$

$$\frac{G^*}{G_m} = 1 - \frac{15(1-\upsilon_m)\left(1-\frac{G_v}{G_m}\right)}{7-5\upsilon_m+2(4-5\upsilon_m)\frac{G_{vp}}{G_m}}\phi_v \qquad \textit{(F-24)}$$

and for the very large concentration limit in Equations F-25 and F-26:

$$\frac{K^*}{K_v} = 1 - \frac{\left(1-\frac{K_m}{K_v}\right)\left[2(1-2\upsilon_m)+(1+\upsilon_m)\frac{K_v}{K_m}\right]}{3(1-\upsilon_m)}(1-\phi_v) \qquad \textit{(F-25)}$$

$$\frac{G^*}{G_v} = 1 - \frac{\left(1-\frac{G_m}{G_v}\right)\left[7-5\upsilon_m+2(4-5\upsilon_m)\frac{G_v}{G_m}\right]}{15(1-\upsilon_m)}(1-\phi_v) \qquad \textit{(F-26)}$$

Hashin (1962) does observe that if the difference between the moduli of the matrix and inclusions is very small then the above Equations F-23 to F-26 approximate to the volumetric mixture rule for moduli in Equation 4-4.

In order to generate an alternative solution that also lies between the upper and lower bounds determined by Hashin, a Bezier curve fit (see Appendix D) was used to interpolate between the small and large concentration straight-line approximations that result from Hashin’s equations (Equations F-23 to F-26).

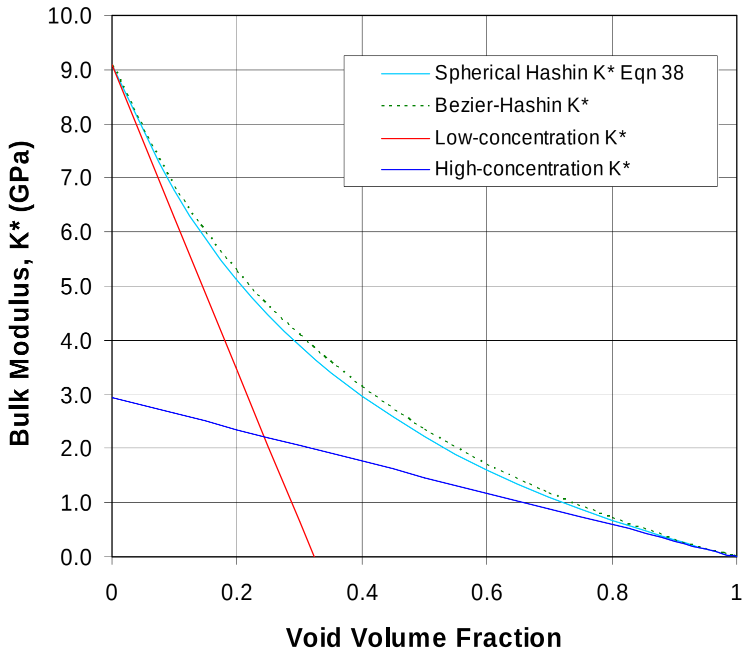

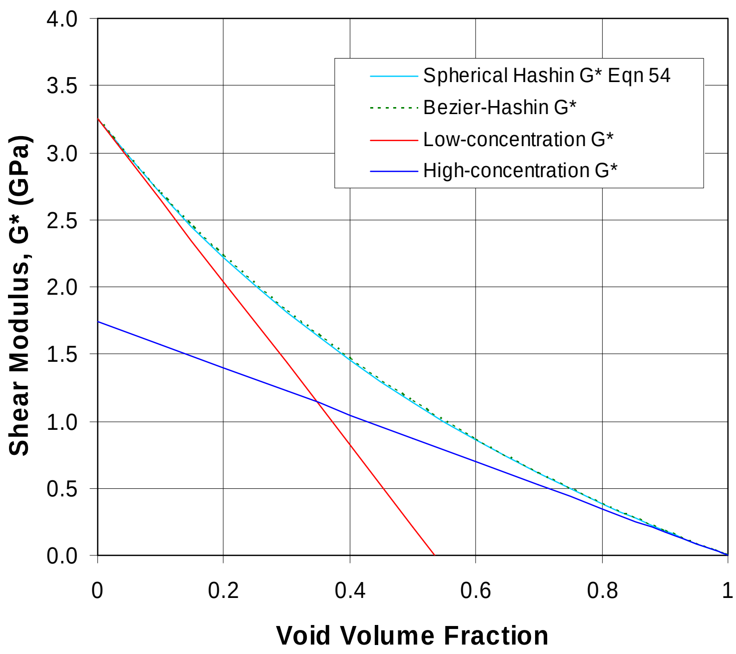

Figure F-6. Comparison of Hashin's proposed equations for bulk and shear modulus with Bezier fits to the high and low-concentration solutions. The equations identified in the legends refer to equations in Hashin (1962).

Bulk and shear moduli are combined to give compression modulus M using:

$$M = K + \frac{4}{3}G$$

Figure F-7 shows a comparison with the simple volumetric model where M_c and M_v are the compression moduli in the composite and air respectively:

$$M^*_{simple} = M_v \phi_v + M_c (1 - \phi_v)$$

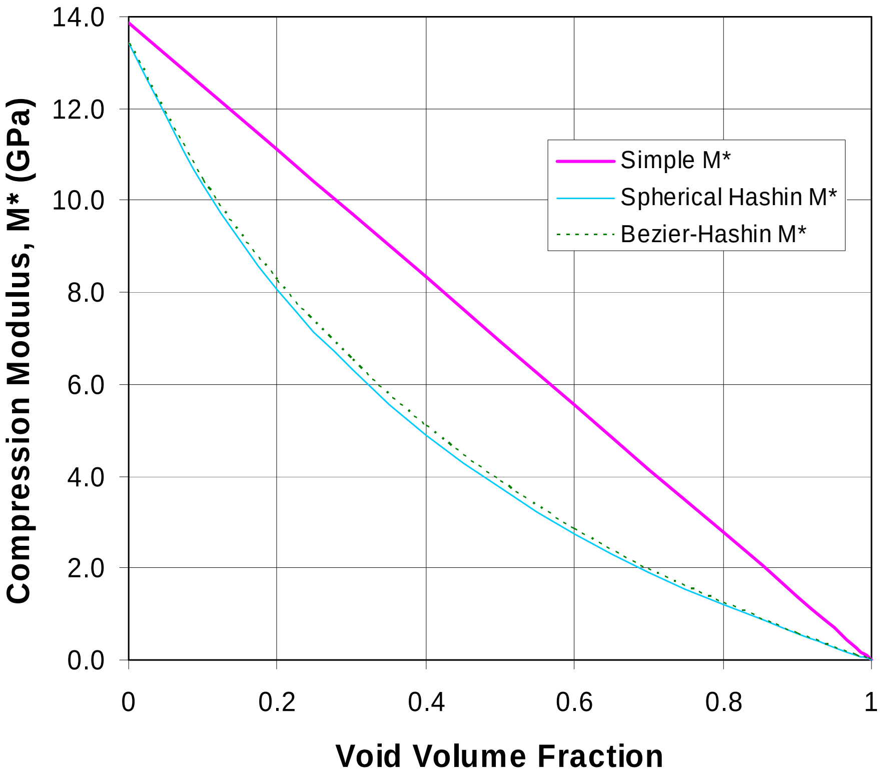

Figure F-7. Comparison of the derived Hashin (1962) compression modulus M with a Bezier fit to the high and low-concentration approximations and the simple volumetric model.*

It has been assumed that porosity effectively replaces both resin and fibres according to the proportion in which they already exist in the composite. The basis for this assumption is that in micrographs of porous regions, the voids do not change the fibre volume fraction of the surrounding composite (see Figure F-8). This suggests that the fibres are not pushed aside by the voids but actually pass through the voids. As very little ultrasound can penetrate into a void, even along the fibres, the fibres have effectively been removed from the local mixture in the same way that the resin has.

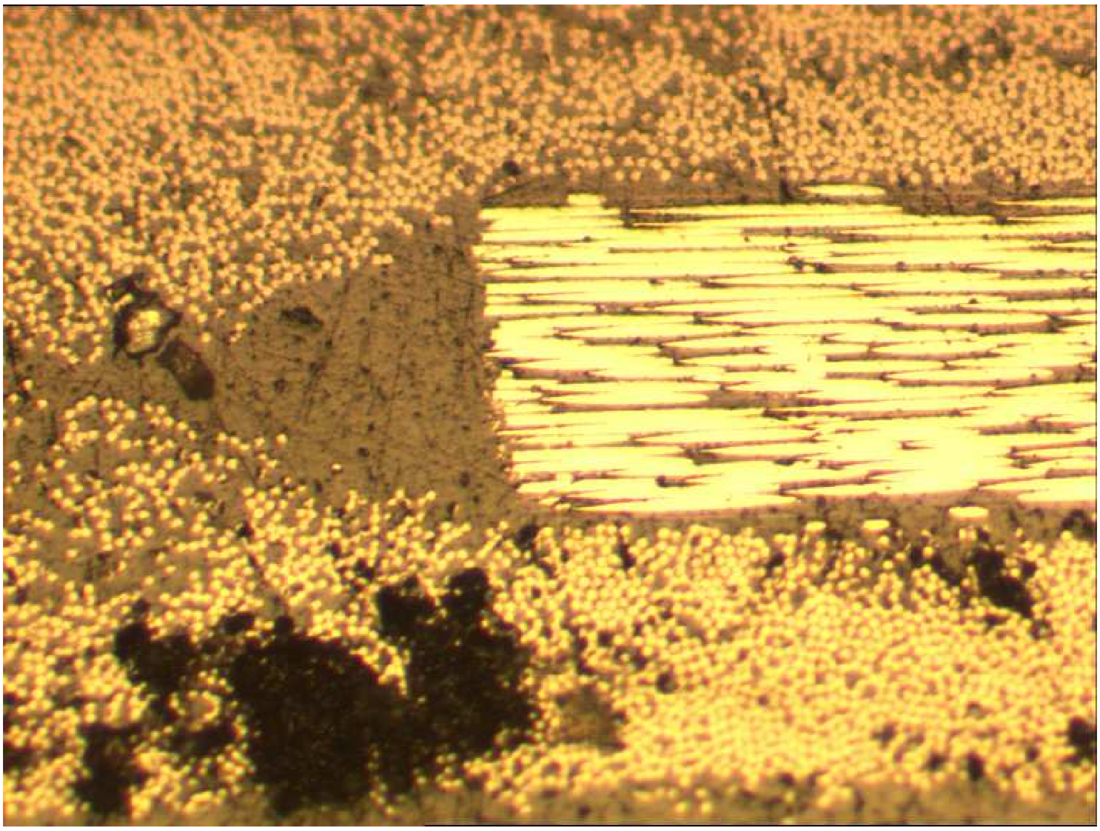

Figure F-8. An example of a micrograph of porosity (black) in a fibre-resin composite near the end of a ply. Note that there is little difference in fibre volume fraction adjacent to the porosity, implying that fibres are not pushed aside by the porosity, but they probably go through the voids.

In the case of porosity, the error shown in Figure F-7 due to using a simple mixture rule compared with the more complex Hashin-Bezier rule is clearly significant. It is illustrated for phase velocity and acoustic impedance in Figure F-9.

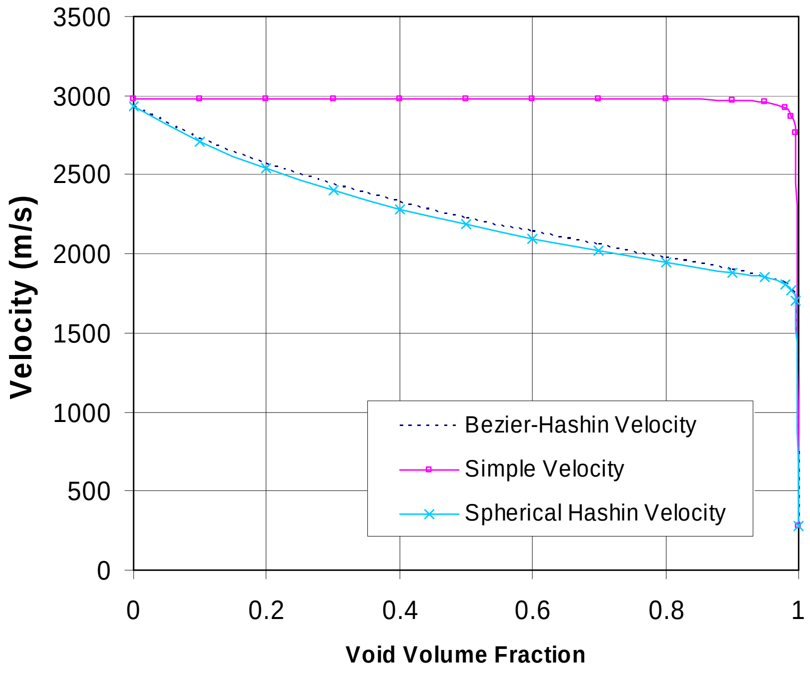

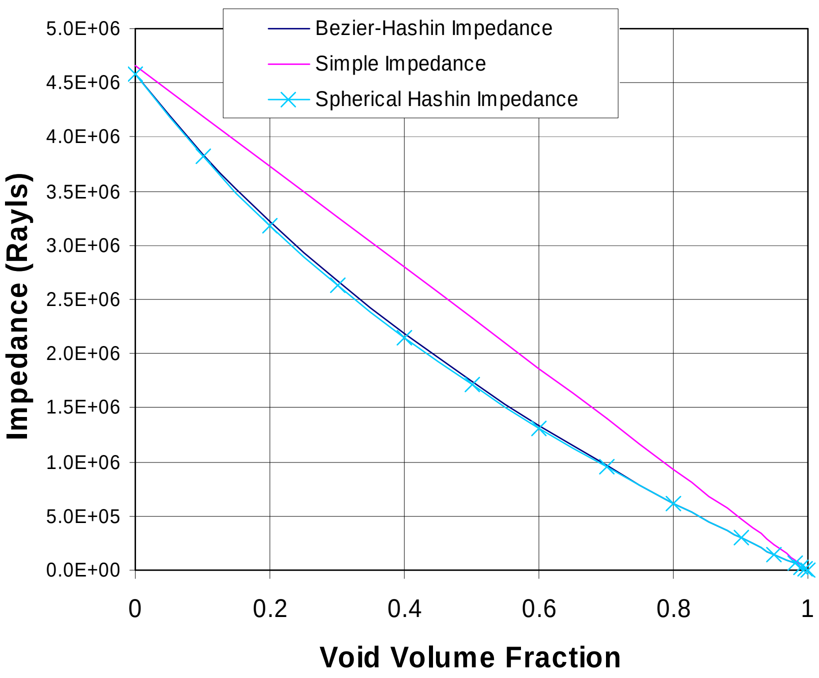

Figure F-9. A comparison of the simple volumetric mixture rule with the Spherical-Hashin equations and the Hashin-Bezier mixture-rule method on phase velocity (top) and acoustic impedance (bottom) as a function of void volume fraction in a 60% fibre volume fraction carbon-fibre composite. Note the significant velocity change in the Spherical-Hashin and Hashin-Bezier models that is not exhibited by the simple volumetric mixture rule.

F.6.2 *Pinfield scattering mixture rule*

Pinfield et al (2010) has presented a treatment of a layer of porosity where the backscattered signals from the pores can be integrated over a random distribution of pores in a layer to determine the frequency-dependent backscattering cross-section. The layer can then be represented as an equivalent medium with a complex impedance, the imaginary part of which accounts for the frequency-dependent backscattering process. Spherical and cylindrical pores are dealt with and the backscattering amplitude includes consideration of the morphology type of the pores. Pinfield calculates that the ratio of the complex impedance of the porous effective medium to the impedance of the porosity-free medium, $\hat{z}$, is given by:

$$\hat{z} \approx \left[1 + iNf_\pi D(k)\right] \tag{F-27}$$

where N is the density of scatterers, f_π is the backscattering amplitude (scattering amplitude at angle π radians) and $D(k)$ is the diffraction correction, which for a plane piston source is calculated to be:

$$D(k) = \frac{\pi b^2}{kz_{\min}} \tag{F-28}$$

where b is the transducer radius, k is the wavenumber and z_{min} is the distance from the transducer to the layer (hence kz_{min} is the phase path length in radians). However, Pinfield does not provide a diffraction correction appropriate for focused transducers.

For spherical scatterers:

$$f_\pi = f(\pi) = \frac{1}{ik}\sum_{n=0}^{\infty}(2n+1)A_n(-1)^n \tag{F-29}$$

and for cylindrical scatterers:

$$f_\pi = f(\pi) = \sqrt{\frac{4}{i\pi k}}\sum_{n=-\infty}^{+\infty}A_n(-1)^n \tag{F-30}$$

where A_n is the scattering coefficient for the nth partial wave order, given by the following approximations:

$$A_0 = i\,(ka)^3 \frac{\left(1-4\eta^2/3\right)}{4\eta^2} \approx \frac{2}{3} i\,(ka)^3 \qquad \textit{(F-31)}$$

$$A_1 = -\frac{1}{9} i\,(ka)^3 \qquad \textit{(F-32)}$$

$$A_2 = i\,(ka)^3 \frac{4\eta^2}{3\left(9-4\eta^2\right)} \approx \frac{1}{24} i\,(ka)^3 \qquad \textit{(F-33)}$$

where a is the pore radius and η is the ratio of shear to compressional wave velocities.

This was implemented in the QQ/UoN model and the front and back of the porous layer give signals that vary with void volume fraction, ϕ_V but not with pore radius, a even though I am using the pore size to calculate f_π and N. The effect of pore size on these two parameters cancels out because N is the void volume fraction ϕ_V divided by the pore size $(4\pi a^3/3)$ and from Equations F-29, F-31, F-32 and F-33, $f_\pi = 29k^2a^3/24$, so

$$Nf_\pi = 29\phi_v k^2/(32\pi)$$

and the whole Equation F-34 for impedance ratio $\hat{z}$ with spherical pores and a planar probe becomes:

$$\hat{z} \approx \left[1 + iNf_\pi D(k)\right] = 1 + i\frac{29\phi_v k}{32}\frac{b^2}{z_{\min}} \qquad \textit{(F-34)}$$

A comparison of the Pinfield et al (2010) model with the Hashin (1962) spherical-inclusion model is shown in Figure F-10, illustrating the enhanced frequency dependence due to the backscattering from porosity included in the Pinfield model.

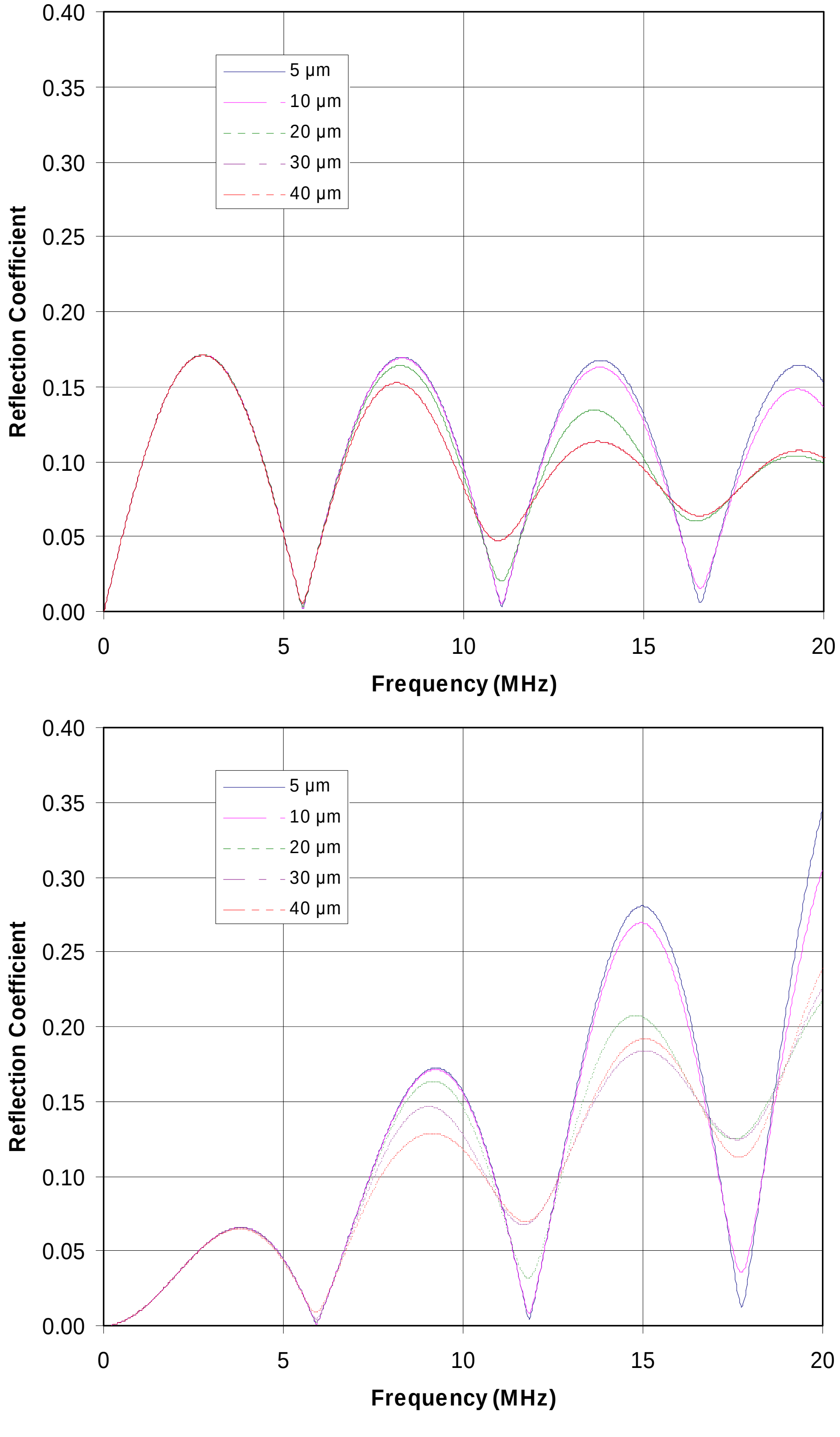

Figure F-10. Comparison of Hashin (1962) spherical-inclusion model (top) with the Pinfield et al (2010) scattering model (bottom) for different pore radii (shown in the legends). In both cases 60% fibre volume fraction carbon-fibre composite was used, containing a single 0.25 mm porous layer with 10% porosity.

F.7 Isotropic fibres in isotropic media

When fibres are present in an isotropic medium, the composite thus formed can still be assumed to be 'transversely isotropic' – properties not varying with angle around an axis in the fibre direction. But the 'longitudinal' properties (in the fibre direction) will be different to the transverse properties. For isotropic fibre material (eg glass or silica) the treatment is simpler than for anisotropic fibres (carbon or graphite). For the purposes of this cartesian-coordinate analysis, fibres will be assumed to be placed in the '3' direction, although some authors use the '1' direction for fibres.

F.7.1 Hashin and Rosen

Hashin and Rosen (1964) and Hashin (1965), using the composite cylinder assemblage (CCA) model, developed expressions for the lower and upper bounds using infinitely long elements of either hexagonal or circular cross-section, each containing a single fibre surrounded by matrix material. For plane-strain bulk modulus (transverse bulk modulus), again the bounds coincide (Equation F-35), but not for shear modulus (Equations F-36 to F-39).

$$\frac{K^*}{K_m} = 1 - \frac{(K_m + G_m)\left(1 - \frac{K_f}{K_m}\right)\phi_f}{K_f + G_m + (K_m - K_f)\phi_f} \qquad \textit{(F-35)}$$

For transverse shear modulus G_T in a plane perpendicular to the fibres, the following equations for the lower and upper bounds apply respectively:

$$\frac{G_T^-}{G_m} = 1 + 2\frac{(K_m + G_m)(G_f - G_m)\phi_f}{K_m(G_m + G_f) + 2G_mG_f - (G_f - G_m)(K_m + 2G_m)\phi_f} \qquad \textit{(F-36)}$$

$$\frac{G_T^+}{G_f} = 1 + 2\frac{(K_f + G_f)(G_m - G_f)\phi_m}{K_f(G_f + G_m) + 2G_fG_m - (G_m - G_f)(K_f + 2G_f)\phi_m} \qquad \textit{(F-37)}$$

and in a plane parallel to the fibres (ie a plane normal to direction 1, shearing in direction 3), these equations for the lower and upper bounds of the axial shear modulus G_A apply respectively:

$$\frac{G_A^-}{G_m} = \frac{G_f + G_m + (G_f - G_m)\phi_f}{G_f + G_m - (G_f - G_m)\phi_f} \tag{F-38}$$

$$\frac{G_A^+}{G_f} = \frac{G_m + G_f + (G_m - G_f)\phi_m}{G_m + G_f - (G_m - G_f)\phi_m} \tag{F-39}$$

F.7.2 Whitney and Riley

Whitney and Riley (1966) claim their work is analogous to that of Hashin and Rosen, but is less rigorous mathematically. They use a repeating cylinder approach but do not specify how the cylinders are packed in the material. They calculate longitudinal and transverse Young's modulus separately, but quote Hashin and Rosen (1964) with a single equation for shear modulus - even though Hashin and Rosen specify upper and lower bounds. At another point in the paper, Whitney and Riley state that they are using the upper bound of Hashin and Rosen's shear modulus because it is more accurate, and yet the equation they quote is actually based on the lower bound Equation F-38 for shear modulus parallel to the fibre direction. The predicted response (see Figure F-11) also matches the lower bound for shear modulus parallel to the fibre direction. Later, Datta et al (1984) showed that the lower bound is appropriate when the fibre shear modulus is larger than the matrix, and the upper bound is when the fibre shear modulus is smaller than the matrix.

Whitney and Riley (1966) derive their own equation (Equation 46 in their paper) for plane-strain bulk modulus (see Equation F-40), which has a minus-sign error in the numerator because when the fibre volume fraction is 100% the modulus should equal the modulus of the fibre and it does not.

Incorrect Eqn 46:

$$K^* = \frac{K_m(K_f + G_m) - G_m(K_f - K_m)\phi_f}{K_f + G_m - (K_f - K_m)\phi_f} \tag{F-40}$$

By correcting Equation F-40 to Equation F-41 and manipulating it (Equations F-42 and F-43) the corrected version can be seen to be identical to the lower bound Equation F-35 from the Hashin and Rosen model (see Figure F-12).

Corrected version: $$K^* = \frac{K_m(K_f + G_m) + G_m(K_f - K_m)\phi_f}{K_f + G_m - (K_f - K_m)\phi_f} \quad \text{(F-41)}$$

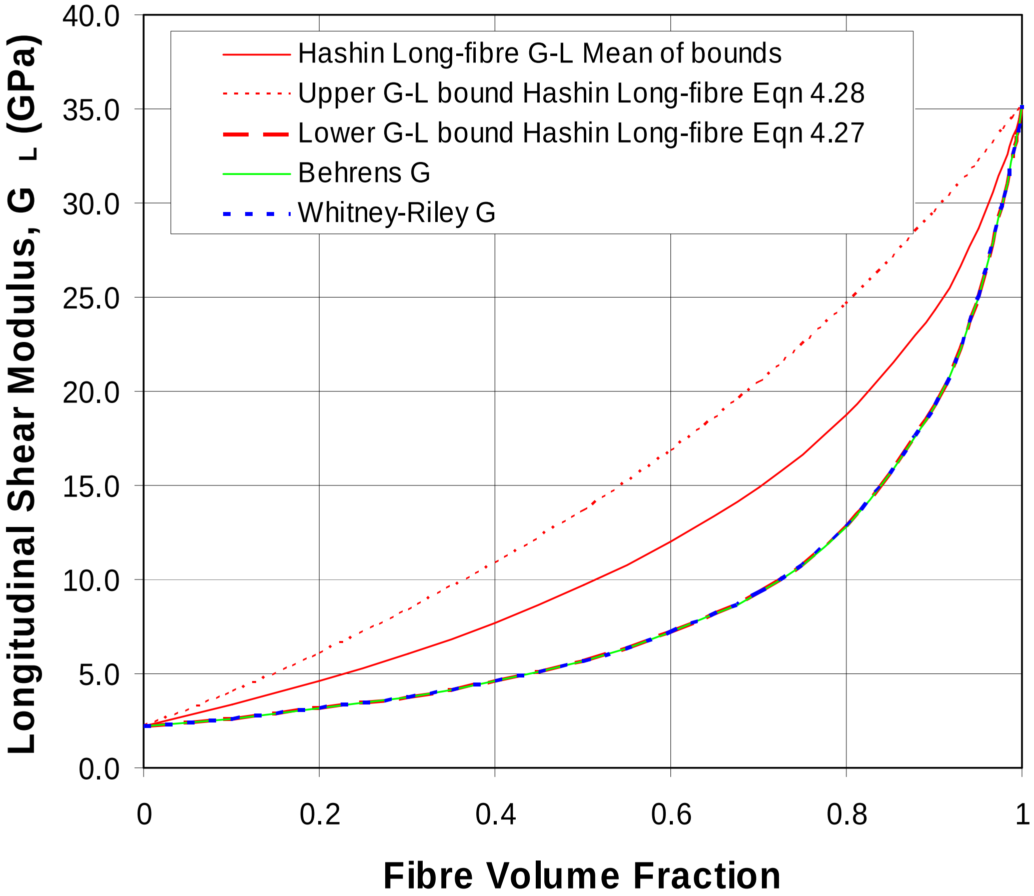

Figure F-11. Comparison of shear modulus predictions for a plane parallel to the fibres from the models of: Hashin (1965), Behrens (1968) and Whitney and Riley (1966) for S-glass-fibre epoxy-resin composite. The Hashin model predicts lower and upper bounds, which are illustrated together with the mean of these two bounds. The legend shows equation numbers from Hashin (1965).

$$K^* = \frac{K_m(K_f + G_m) + K_m(K_m - K_f)\phi_f - (K_m + G_m)(K_m - K_f)\phi_f}{K_f + G_m + (K_m - K_f)\phi_f} \quad \text{(F-42)}$$

$$K^* = K_m - \frac{(K_m + G_m)(K_m - K_f)\phi_f}{K_f + G_m + (K_m - K_f)\phi_f} \quad \text{(F-43)}$$

This is also incorrect when quoted in Appendix A of Zimmer and Cost (1969).

There are further errors in Whitney and Riley (1966) in the definition of the bulk modulus of fibre and matrix where an incorrect conversion from Young's modulus and Poisson's ratio is stated. It should be $K=E/3(1-2\nu)$.

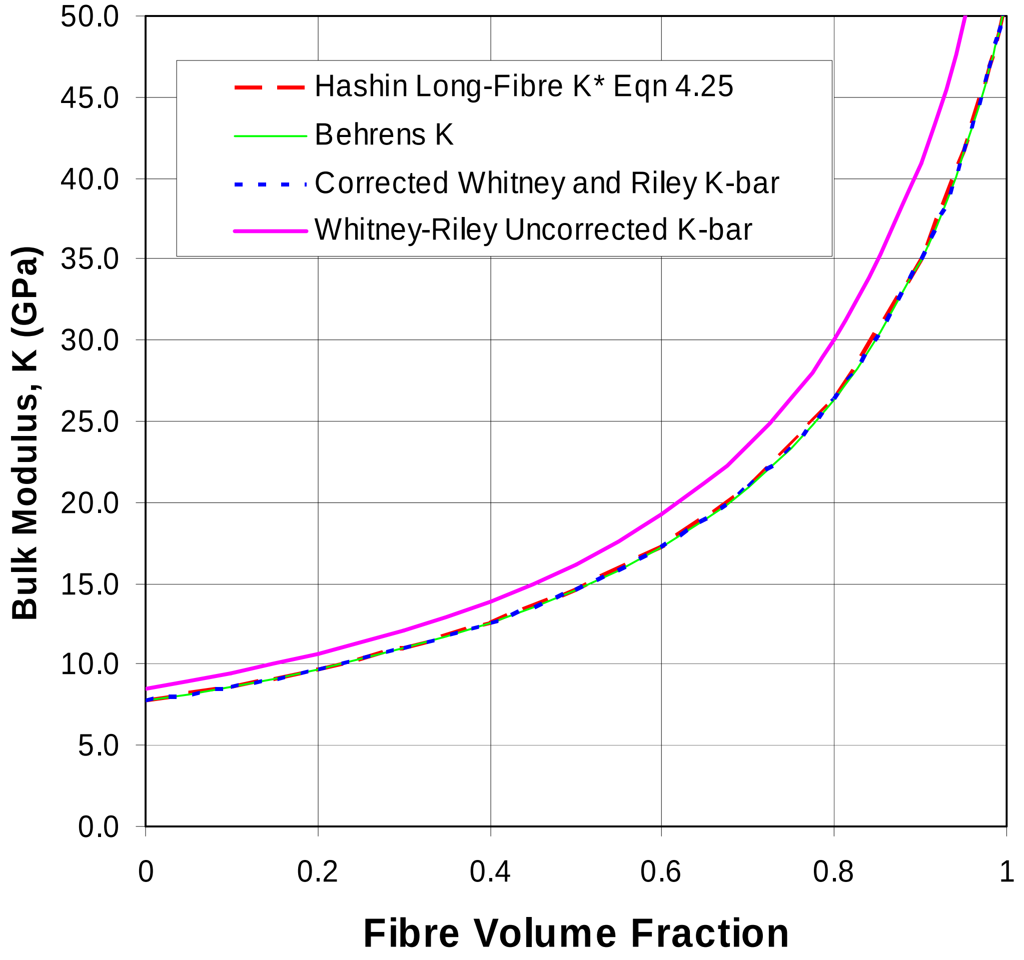

Figure F-12. Comparison of plane-strain bulk modulus predictions from the models of: Hashin (1965), Behrens (1968) and the corrected Whitney and Riley (1966) for S-glass-fibre epoxy-resin composite. Also shown is the Whitney and Riley prediction after correcting the sign error but before correcting the derivations of K from E and ν.

F.7.3 Greszczuk

Greszczuk (1966) modelled a rectangular array of circular filaments embedded in a continuous elastic matrix, rather than using repeating composite elements. Potentially this is a more realistic method but it too ignores any interaction between fibres and matrix. Greszczuk also generated separate expressions for longitudinal (in fibre direction) and transverse Young's modulus. Greszczuk compared his equations (Equations F-44 to F-54) with "a more rigorous method" apparently using numerical methods and claimed agreement within 10% in the range 50% to 73% fibre volume fraction. However, above 91% fibre volume fraction the Geszczuk equations become unstable (see Figure F-13). 90.7% is the maximum volume fraction possible for hexagonally packed cylindrical fibres, so the discontinuity may be caused by this effect.

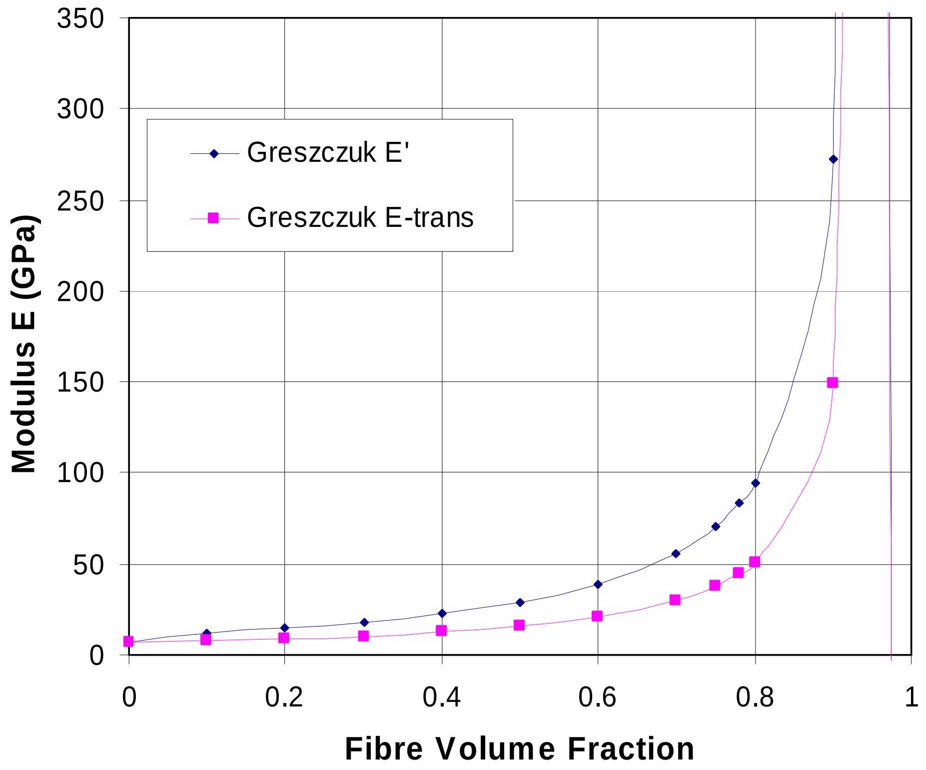

Figure F-13. Transverse Young's Modulus (E-trans) and an intermediate modulus (E') calculated from the equations in Greszczuk (1966), showing the discontinuity above 90.7% fibre volume fraction.

$$E_L = E_f \phi_f + E_m (1 - \phi_f) \tag{F-44}$$

$$E_T = E_0 \beta + E_m^* (1 - \beta) \tag{F-45}$$

$$\nu_{LT} = \nu_f \phi_f + \nu_m (1 - \phi_f) \tag{F-46}$$

$$\nu_{TL} = \nu_{LT} \left(\frac{E_T}{E_L} \right) \tag{F-47}$$

$$G_{LT} = G_0\beta + G_m^*(1-\beta) \tag{F-48}$$

where:

$$E_0 = \frac{E_m^* + 2\beta(E_f - E_m^*)}{1 + \dfrac{2\beta(1-2\beta)}{E_m^* E_f}\left[(E_f - E_m^*)^2 - (\nu_m E_f - \nu_f E_m^*)^2\right]} \tag{F-49}$$

$$G_0 = \frac{G_m^* G_f}{G_f + 2\beta(G_m^* - G_f)} \tag{F-50}$$

$$E_m^* = \frac{E_m}{1-\nu_m^2} \tag{F-51}$$

$$G_m^* = \frac{G_m}{1 - \dfrac{2\nu_m^2}{1-\nu_m}} \tag{F-52}$$

$$\beta = \sqrt{\frac{\phi_f}{\pi}} \tag{F-53}$$

$$M_T = E_T \frac{1-\nu}{(1+\nu)(1-2\nu)} \tag{F-54}$$

The discontinuity shown in Figure F-13 occurs when the denominator of Equation F-49 tends to zero, which occurs when:

$$E_m^* E_f + 2\beta(1-2\beta)\left[(E_f - E_m^*)^2 - (\nu_m E_f - \nu_f E_m^*)^2\right] \to 0 \tag{F-55}$$

which is equivalent to

$$2\beta(1-2\beta) + \frac{E_m^* E_f}{(E_f - E_m^*)^2 - (\nu_m E_f - \nu_f E_m^*)^2} \to 0 \tag{F-56}$$

or:

$$4\beta^2 - 2\beta - \frac{E_m^* E_f}{(E_f - E_m^*)^2 - (\nu_m E_f - \nu_f E_m^*)^2} \to 0 \tag{F-57}$$

Using the quadratic formula:

$$\beta = \frac{2 \pm \sqrt{4 + 16\dfrac{E_m^* E_f}{(E_f - E_m^*)^2 - (\nu_m E_f - \nu_f E_m^*)^2}}}{8} \qquad \textit{(F-58)}$$

which is equivalent to:

$$4\beta = 1 \pm \sqrt{1 + 4\frac{E_m^* E_f}{(E_f - E_m^*)^2 - (\nu_m E_f - \nu_f E_m^*)^2}} \qquad \textit{(F-59)}$$

At present it is not clear whether there is an error that has caused this discontinuity, or a genuine physical reason. It is beyond the scope of this study to pursue this any further.

F.7.4 Behrens

Behrens (1967a; 1967b; 1969a; 1969b) developed an independent model using rectangular symmetry which produces an identical equation to Hashin (1965) for the bulk modulus, but a single equation for the shear modulus. This shear modulus must be for shear modulus parallel to the fibres because it matches Whitney and Riley's and is equivalent to the lower bound of Hashin (1965) - see Figure F-11 - once it is corrected to the version that Smith (1972) quotes (equation 8b of his paper) – apparently correcting a mistake in equation (64) of Behrens (1969a), but without stating that it is a correction.

F.8 Anisotropic fibres in an isotropic matrix

Carbon and graphite fibres are anisotropic, whereas glass fibres are isotropic. Various papers have extended the above work to anisotropic fibres and some have also considered an anisotropic matrix such as in carbon-carbon composites.

F.8.1 Behrens

Behrens (1967a; 1967b; 1969a; 1969b; 1971) considered anisotropic fibres in an anisotropic matrix and derived equations for the stiffness matrix components in terms of the Lamé parameters for the fibre and matrix. He assumed cylindrical point symmetry for the individual fibres, and thus transverse isotropy of the composite. The expressions generated by Behrens were subsequently quoted by R E Smith (1972) in a form that is more consistent with the nomenclature of this appendix and so they will be presented below. They were also subsequently quoted by Martin (1977) in a slightly different form.

F.8.2 Smith (1972)

R E Smith (1972) quotes Behrens's (1969a) equations for bulk and shear modulus (assumed to be transverse bulk and transverse shear moduli), as well as for the C_{33} and C_{13} parameters as follows, with a correction in the fourth equation for C_{13} (the matrix $C_{13,m}$ was referred to instead of the fibre $C_{13,f}$ in the numerator):

$$K_T = \phi_m K_m + \phi_f K_f - \frac{(K_f - K_m)^2 \phi_m \phi_f}{\phi_m K_f + \phi_f K_m + G_m} \tag{F-60}$$

$$G_T = \phi_m G_m + \phi_f G_f - \frac{(G_f - G_m)^2 \phi_m \phi_f}{\phi_m G_f + (1+\phi_f) G_m} \tag{F-61}$$

$$C_{33} = \phi_m C_{33,m} + \phi_f C_{33,f} - \frac{(C_{13,f} - C_{13,m})^2 \phi_m \phi_f}{\phi_m K_f + \phi_f K_m + G_m} \tag{F-62}$$

$$C_{13} = \phi_m C_{13,m} + \phi_f C_{13,f} - \frac{(C_{13,f} - C_{13,m})(K_f - K_m) \phi_m \phi_f}{\phi_m K_f + \phi_f K_m + G_m} \tag{F-63}$$

F.8.3 Silnutzer (1972)

In a PhD thesis, Silnutzer (1972) moved from what are essentially second-order bounds in the Hashin (1965) and Hill (1964) treatments to third-order bounds because they are exact up to the third order in the difference in the phase properties. The expressions derived are considerably more complex involving evaluation of integrals. An example of the simplified version of these expressions quoted by Torquato and Lado (1992) is given here:

$$K_T^+ = \phi_m K_m + \phi_f K_f - \frac{(K_f - K_m)^2 \phi_m \phi_f}{\phi_m K_f + \phi_f K_m + \zeta_m G_m + \zeta_f G_f} \qquad \textit{(F-64)}$$

where ζ_m and ζ_f are microstructural parameters defined as triple integrals related to probabilities of finding certain morphologies in the matrix or fibre phases respectively.

F.8.4 Martin (1977)

Martin (1977) clearly distinguishes between isotropic fibres and anisotropic fibres. For anisotropic fibres he quotes R E Smith (1972) and Behrens (1969a) with equations in a different form, by making some assumptions that the matrix will be isotropic and so $C_{13,m} = C_{12,m}$; $C_{11,m} = C_{33,m}$; $G_m = C_{44,m}$; that the bulk modulus of the matrix, $K_m = ½(C_{11,m} + C_{12,m})$ and the transverse fibre bulk modulus, $K_f = ½(C_{11,f} + C_{12,f})$, this time correcting a sign error in the denominator of the first equation:

$$C_{33} = \phi_m C_{11,m} + \phi_f C_{33,f} - \frac{2(C_{13,f} - C_{12,m})^2 \phi_m \phi_f}{(C_{11,f} + C_{12,f})\phi_m + (C_{11,m} + C_{12,m})\phi_f + 2C_{44,m}} \qquad \textit{(F-65)}$$

$$C_{13} = \phi_m C_{12,m} + \phi_f C_{13,f} - \frac{(C_{13,f} - C_{13,m})(C_{11,f} + C_{12,f} - C_{11,m} - C_{12,m})\phi_m \phi_f}{(C_{11,f} + C_{12,f})\phi_m + (C_{11,m} + C_{12,m})\phi_f + 2C_{44,m}} \qquad \textit{(F-66)}$$

By inspection, using the assumed equivalences, these equations can now be seen to be equivalent to those of R E Smith (1972) and Behrens (1969a) shown in Equations F-62 and F-63.

F.8.5 Hashin (1979)

Hashin (1979) extends Hashin and Rosen (1964) and Hashin (1965) to allow for carbon and graphite fibres, which are highly anisotropic. In fact the expressions for transverse bulk modulus, transverse shear modulus and axial shear modulus are identical in form to those in Hashin (1965) except that they are more specific about which moduli in the constituent materials should be used. For example, the expression for transverse bulk modulus K_T requires the use of the bulk moduli for fibre and matrix and the shear modulus for the matrix (see

Equation F-35) and these are specified in Hashin (1979) as the *transverse* moduli. For the transverse shear modulus G_T (Equations F-36 and F-37) again it is the *transverse* moduli in either the matrix or the fibre that are required. However, for the axial shear modulus, G_A (Equations F-38 and F-39) the *axial* shear moduli in matrix and fibre need to be substituted. So the expressions become:

$$\frac{K_T}{K_{Tm}} = 1 - \frac{(K_{Tm} + G_{Tm})\left(1 - \dfrac{K_{Tf}}{K_{Tm}}\right)\phi_f}{K_{Tf} + G_{Tm} + (K_{Tm} - K_{Tf})\phi_f} \qquad \text{(F-67)}$$

$$\frac{G_T^-}{G_{Tm}} = 1 + 2\frac{(K_{Tm} + G_{Tm})(G_{Tf} - G_{Tm})\phi_f}{K_{Tm}(G_{Tm} + G_{Tf}) + 2G_{Tm}G_{Tf} - (G_{Tf} - G_{Tm})(K_{Tm} + 2G_{Tm})\phi_f} \qquad \text{(F-68)}$$

$$\frac{G_T^+}{G_{Tf}} = 1 + 2\frac{(K_{Tf} + G_{Tf})(G_{Tm} - G_{Tf})\phi_m}{K_{Tf}(G_{Tf} + G_{Tm}) + 2G_{Tf}G_{Tm} - (G_{Tm} - G_{Tf})(K_{Tf} + 2G_{Tf})\phi_m} \qquad \text{(F-69)}$$

$$\frac{G_A^-}{G_{Am}} = \frac{G_{Af} + G_{Am} + (G_{Af} - G_{Am})\phi_f}{G_{Af} + G_{Am} - (G_{Af} - G_{Am})\phi_f} \qquad \text{(F-70)}$$

$$\frac{G_A^+}{G_{Af}} = \frac{G_{Am} + G_{Af} + (G_{Am} - G_{Af})\phi_m}{G_{Am} + G_{Af} - (G_{Am} - G_{Af})\phi_m} \qquad \text{(F-71)}$$

F.8.6 Datta et al (1984)

Datta et al (1984) consider random but homogeneous distributions of identical long and parallel fibres and the propagation of longitudinal and shear waves perpendicular to the fibre direction. A multiple scattering approach is used to determine a dispersion relationship in the long-wavelength limit. Fibres are considered to be anisotropic and the outcome is expressions for elastic constants over the whole range of fibre volume fractions.

The transverse plane-strain bulk modulus expression matches that of Hashin (1965) (see Equation F-35) and the transverse shear modulus matches the lower bound expression of Hashin (1965) (see Equation F-36) when the fibre has a larger shear modulus than the matrix and identical to the upper bound (Equation F-37) when the fibre has a lower shear modulus than the matrix..

The expression obtained for the longitudinal shear modulus (in a plane parallel to the fibres) is identical to that of Hashin (1965) lower bound (see Equation F-38) when the fibre has a larger shear modulus than the matrix and identical to the upper bound (Equation F-39) when the fibre has a lower shear modulus than the matrix.

F.8.7 Chao and Chaturvedi (1997)

Chao and Chaturvedi (1997) developed a new unified framework based on Helmholtz and Gibbs free energy functions, and micromechanical models involving average stresses and strains in the composite using the approach of Eshelby (1957). They compared these with the predictions from Hashin and Rosen (1964) and Tsai and Hahn (1980), producing the graphs shown in Figure F-14 for transverse Young's modulus in a glass-fibre composite (isotropic fibres) and Figure F-15 for transverse Young's modulus in a carbon-fibre composite.

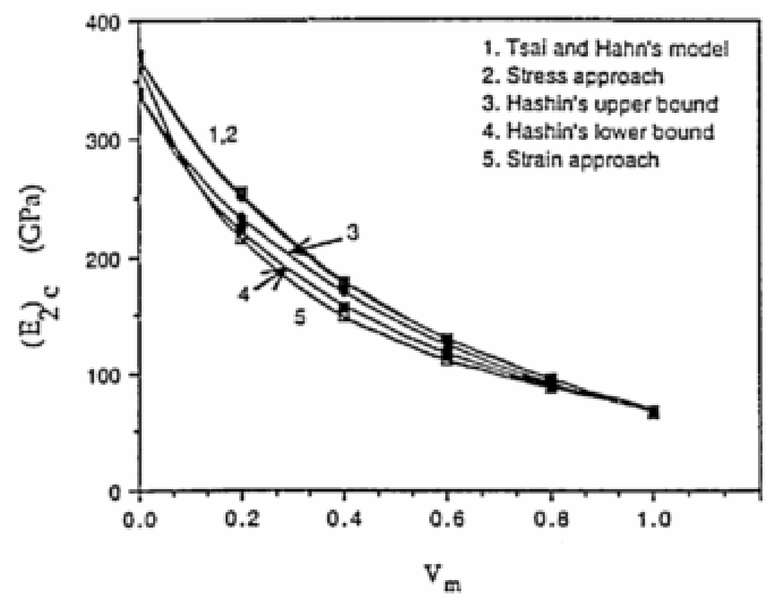

Figure F-14. Graph from Chao and Chaturvedi (1997) showing, for an isotropic (glass) fibre, a comparison of their stress and strain approaches with Hashin and Rosen (1964) and Tsai and Hahn (1980). Note that the horizontal axis is matrix volume fraction.

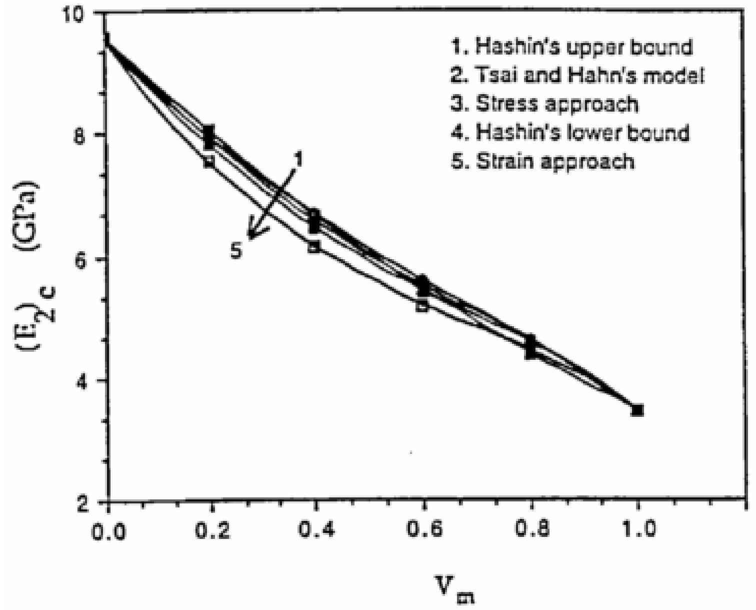

Figure F-15. Graph from Chao and Chaturvedi (1997) showing, for an anisotropic (carbon) fibre, a comparison of their stress and strain approaches with Hashin and Rosen (1964) and Tsai and Hahn (1980). Note that the horizontal axis is matrix volume fraction.

F.9 Summary of chosen equivalent medium models

The result of this assessment of equivalent medium models was that the Hashin (1965) model was used for carbon fibres in resin and the Hashin (1962) spherical-particle model was used for porosity in composite. In addition, an option to use the Pinfield et al (2010) model for porosity was added because it includes the frequency dependence of the backscattering from a given size of pores.

APPENDIX G Simulating Fibre Orientation Images

G.1 Motivation

In order to validate the various fibre-orientation measurement methods for a range of different experimental parameters, it is necessary to use carefully controlled input data and the most efficient method is to simulate the images, which can then be processed using the methods that have been developed for experimental data. By knowing exactly what orientation of fibres was simulated in the image, it is then possible to compare this with the measured orientation over the full range.

G.2 In-plane fibre tows

The main effect allowing in-plane fibre-orientation to be measured from a C-scan of the reflections from a thin slice in a composite is the variation in the reflection amplitude with resin-layer thickness. The resin layer thickness varies due to the fibre-tow lay-up, which introduces undulations in the resin layers spaced at the fibre-tow spacing, which typically can be from 1 mm to 5 mm.

A simulation of these fibre-tow undulations can be introduced in a C-scan image by specifying the fibre orientation and tow spacing and creating cosine-squared variations in the image accordingly (as shown in Figure G-1). A stack of plies with different orientations can then be built up into a 3D profile of C-scans for validation of ply stacking-sequence analysis – see Figure G-1.

It is then possible to create in-plane fibre-waviness of known amounts by simulating a sinusoidal ‘wave’ with a Gaussian envelope – see Figure G-2. The peak simulated deviation in orientation can be calculated because it occurs when the Gaussian envelope is at unity and the sine wave is at maximum gradient. This is very useful for quantitative validation of the in-plane waviness measurements.

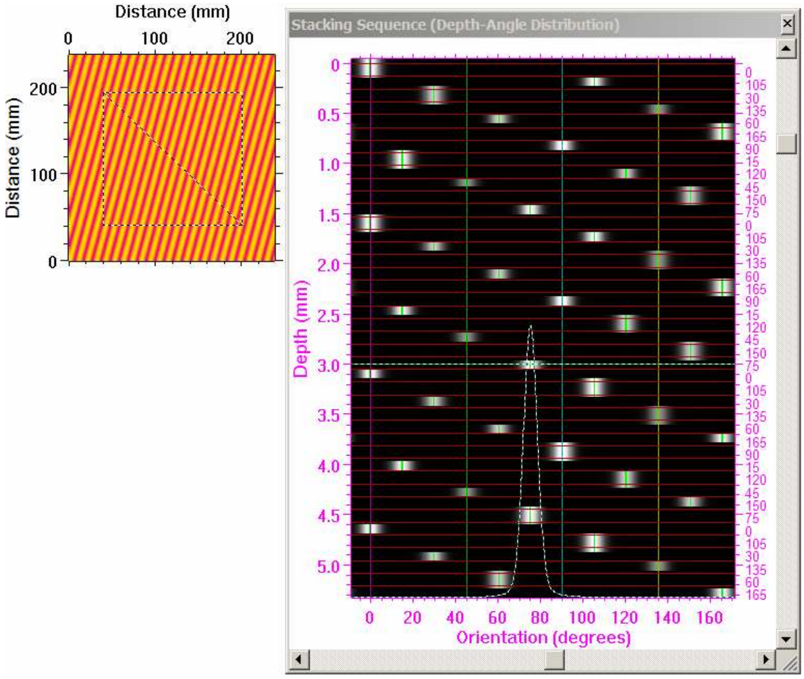

Figure G-1. Simulated in-plane fibre tows of spacing 10 mm and orientation 75º in one C-scan (left), which is one layer from a 3D-profile of C-scans of plies with fibre orientations that step by 15º per ply.

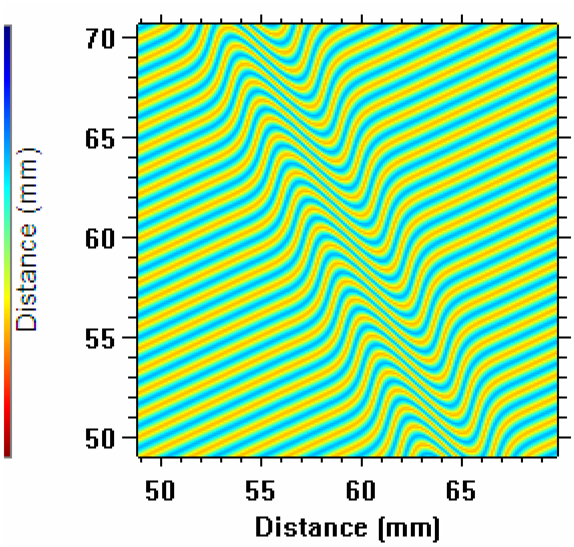

Figure G-2. Simulated in-plane waviness of wavelength 8 mm and amplitude 3 mm, with a Gaussian-envelope 1/e half-width 2 mm, superimposed on a simulated fibre tows of spacing 1 mm and orientation 25º.

A useful outcome of using an equation-generated waviness profile is the ability to calculate the true angle of the profile generated by differentiation of the equation. A Gaussian-enveloped sine wave can be represented by Equation G-1.

$$y = A_0 e^{-x^2 / X_0^2} \cos(\omega_0 x + \theta) \qquad \textit{(G-1)}$$

where: y = y-pixel location

x = x-pixel location

A_0 = vertical scaling factor, (Aspect ratio of y to x)

X_0 = half the width of the envelope at $1/e$ in units of x

ω_0 = $2\pi f_x$ where f_x is $1/T_x$ and T_x is the period in x

θ = phase

An example of the Equation G-1 output is shown in Figure G-3. Then the waviness-profile angle, ϕ, can be calculated for any value of x using Equation G-2.

$$\phi = \arctan\left[-A_0 e^{-x^2 / X_0^2}\left(\omega_0 \sin(\omega_0 x + \theta) + \frac{2x}{X_0^2}\cos(\omega_0 x + \theta)\right)\right] \qquad \textit{(G-2)}$$

The graph in Figure G-3 plots the waviness profile and the associated waviness-profile angle obtained using Equation G-2 with the following settings:

A_0 = 6

X_0 = 20 pixels

T_x = 60 pixels

θ = 90 degrees

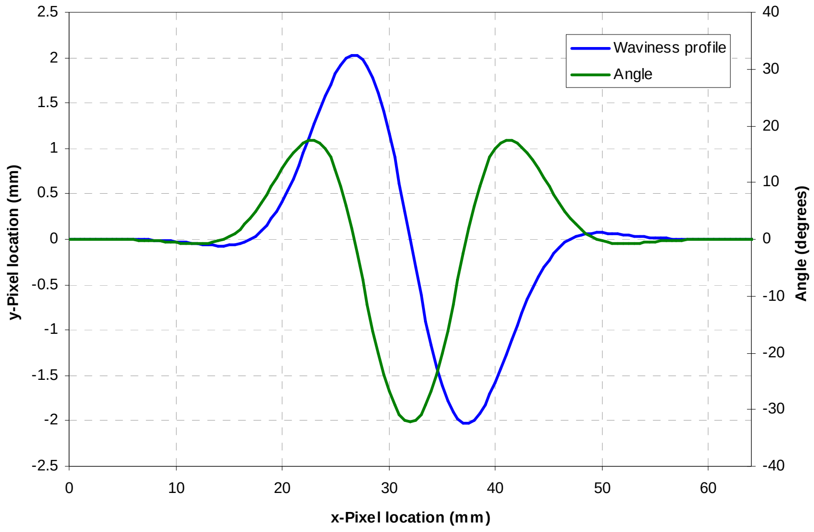

Figure G-3 Waviness profile and associated waviness-profile angle for a waviness profile generated using Equation G-1 with A_0 = *6,* X_0 = *20 pixels,* T_x *= 60 pixels,* θ *= 90 degrees. A Pixel size of 0.5mm was used to convert x-pixel and y-pixel locations into units of millimetres*

The ability to populate an image with a waviness profile generated using Equation 9 has been implemented into ANDSCAN. Thus it is possible to generate a simulated waviness image with a known angular variation as a function of pixel location. It is possible to use ANDSCAN to generate waviness in either a C-scan or a B-scan image.

Simulated C-scan waviness profiles have been used for evaluating the in-plane waviness measurement technique implemented in ANDSCAN, while simulated B-scans have been used for evaluating ANDSCAN's out-of-plane wrinkling measurement method.

G.3 Woven Fabrics

For the Ply Fingerprinting methods that are being proposed for woven fabrics it is important to be able to simulate each weave type as there may be a need to match real fingerprints to simulated fingerprints in order to identify the weave type. Examples of different weave types are shown in Figure G-4.

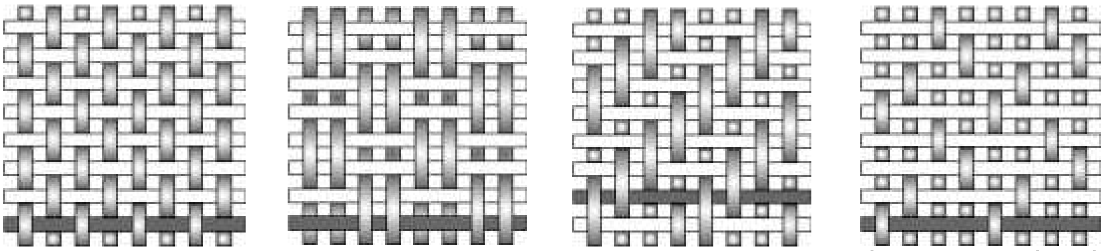

Plain Basket 2*x*2 Twill 2*x*2 4-harness satin with ‘crow’s-foot’ [1,2,3,2] repeat

Figure G-4. Examples of different weave types.

In order to simulate these weaves, the basic fibre-tow simulation algorithm was modified to calculate, at each pixel, its proximity to a fibre tow of the perpendicular orientation. This distance then determines how the pixel is shaded on the basis that the fibre tow will start to turn down under a perpendicular fibre tow and therefore reflect less ultrasound. Examples of simulated C-scans, dominant angles, and angular power distributions are shown in Figure G-5.

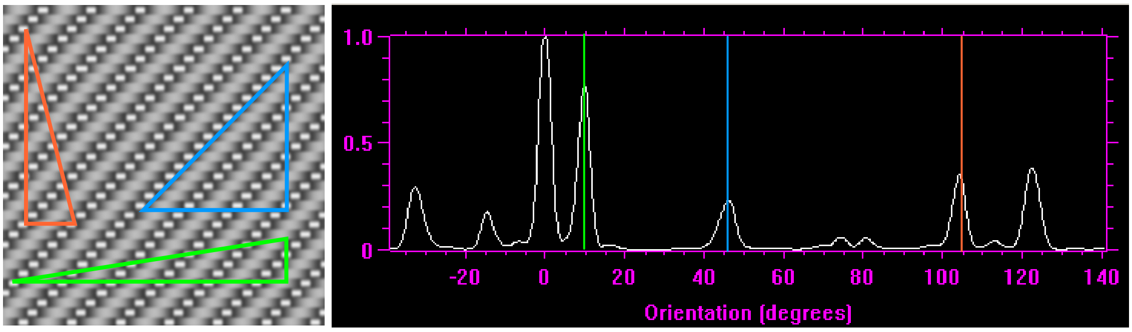

Figure G-5. Simulated 5-harness satin weave, offset [1], and its corresponding 'fingerprint' angular power distribution.

G.4 Out-of-plane plies

For out-of-plane ply B-scan images of wrinkles the simulation has to generate ultrasonic waveforms. The basic building block is a sine wave at the resonant frequency corresponding to the required ply spacing and velocities of the fibre and matrix. This sine wave effectively simulates the inter-ply reflections in the composite and is amplitude modulated by an envelope that simulates the front-wall and back-wall echoes in the composite but goes to zero before and after these strong echoes. The wrinkle itself effectively frequency-modulates the waveform by changing the ply spacing in a controlled way depending on the location of the waveform in the B-scan stack. The wrinkle is also a sine wave multiplied by Gaussian envelopes in both the time axis (depth) and laterally across the B-scan. An example of such a waveform and multiple waveforms forming a B-scan are shown in Figure G-6.

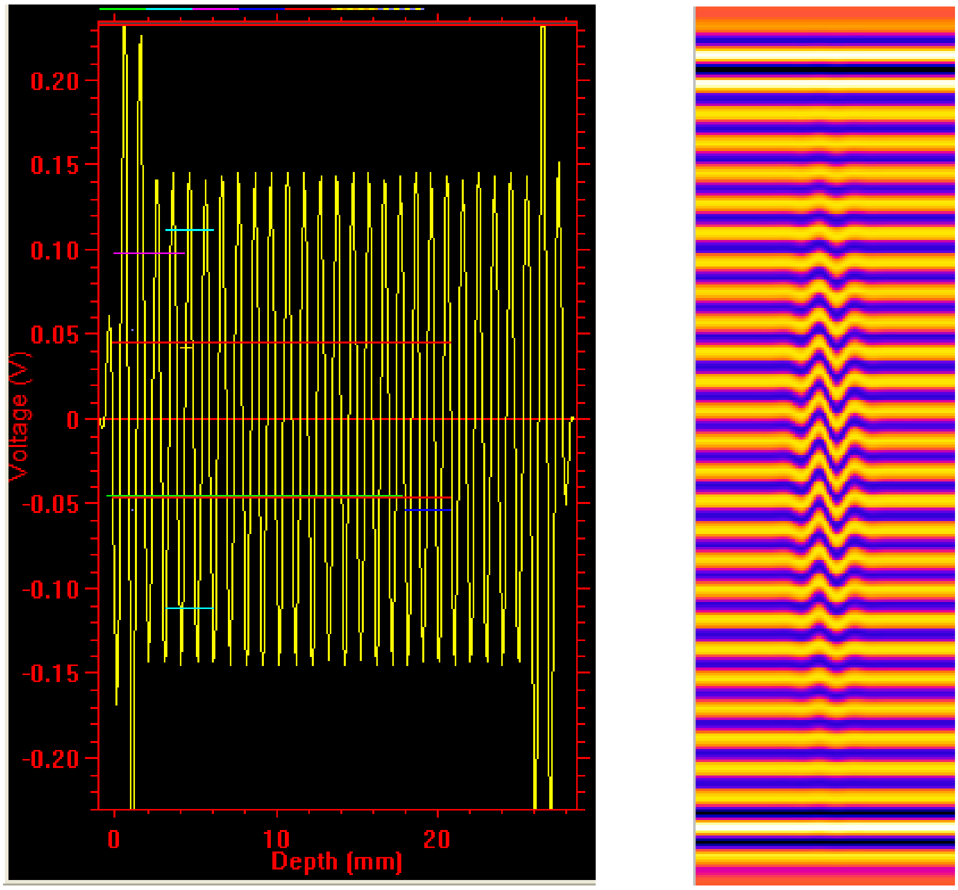

Figure G-6. Simulated waveform (left) and B-scan (right) for a wrinkle.

APPENDIX H Accuracy of fibre orientation measurements

H.1 Introduction

The StackScan toolset encompasses the tools required to measure and map, as a function of 3D location, fibre orientation in carbon-fibre reinforced polymer (CFRP) structures. StackScan requires a full-waveform pulse-echo ultrasonic data set from which three primary types of fibre-orientation measurement are possible:

- Ply stacking sequence
- Out-of-plane ply wrinkling
- In-plane fibre waviness

This appendix deals with the general accuracy of fibre-orientation measurements using the 2D-FFT method with the aim of being able to state an accuracy value that has been validated scientifically. Firstly it is important to differentiate between *accuracy* - the systematic uncertainty in the reported value relative to the true value – and *precision* – the random uncertainty or reproducibility over repeated measurements of the same value. Both are important, but it is accuracy that this appendix addresses, precision being easier to assess and of less concern at the current TRL level.

There are generally multiple contributors to inaccuracy, known as sources of systematic uncertainty. If it is possible to separate these sources then their contributions can be assessed separately and recombined using standard methods. Often, in the course of assessing these sources of error, it is realised that a correction method can be applied to reduce a systematic bias in the data. A good example of this is the correction for angular dependence that was described in Chapter 6. Once the correction is in use, it is possible to assess the accuracy of the corrected output values. Alternatively, it may become clear that particular experimental parameters can be optimised to minimise the uncertainties.

The sources of systematic uncertainty in the measurement of in-plane fibre orientation have been identified as follows in two broad categories:

1. Peak angle measurement from the 2D-FFT of a series of clearly-defined lines at one angle in an image, and how this varies with:
    a. Angle of lines with uniform spacing.
    b. Zero padding and windowing before performing the 2D-FFT
    c. Variable line spacing and harmonics or sub-harmonics of the basic line spacing.
    d. Insufficient pixels between lines to define the spatial frequencies well.
    e. Insufficient lines in the whole image to define the angle.
    f. Number of points in the portion of the image used for the 2D-FFT.
    g. Spatial noise in the image containing the lines.

2. Potential for a real C-scan of a layer in the structure to deviate from a series of clearly-defined lines at one angle:
    a. Smoothing of the lines caused by increased spatial averaging of the sensor.
    b. Presence of lines at other angles from plies above or below
    c. Depth-dependent effects other than in a. or b. above
    d. Waviness in the lines.
    e. Spatial noise in the image.

Although a complete treatment of uncertainties for each of the fibre orientation parameters is beyond the requirements for this project, this appendix records initial work investigating many of the above sources of systematic uncertainty using simulated images, as well as the rationale for a future, more rigorous assessment. Simulated images were used because they allow predictable and measurable variations in each effect to be achieved.

Before presenting this initial uncertainty assessment, it is important to show the characteristics of C-scans from layers in a real composite and the related 2D-FFT and angular power distribution so an example is shown in Figure H-1 for a 45º ply.

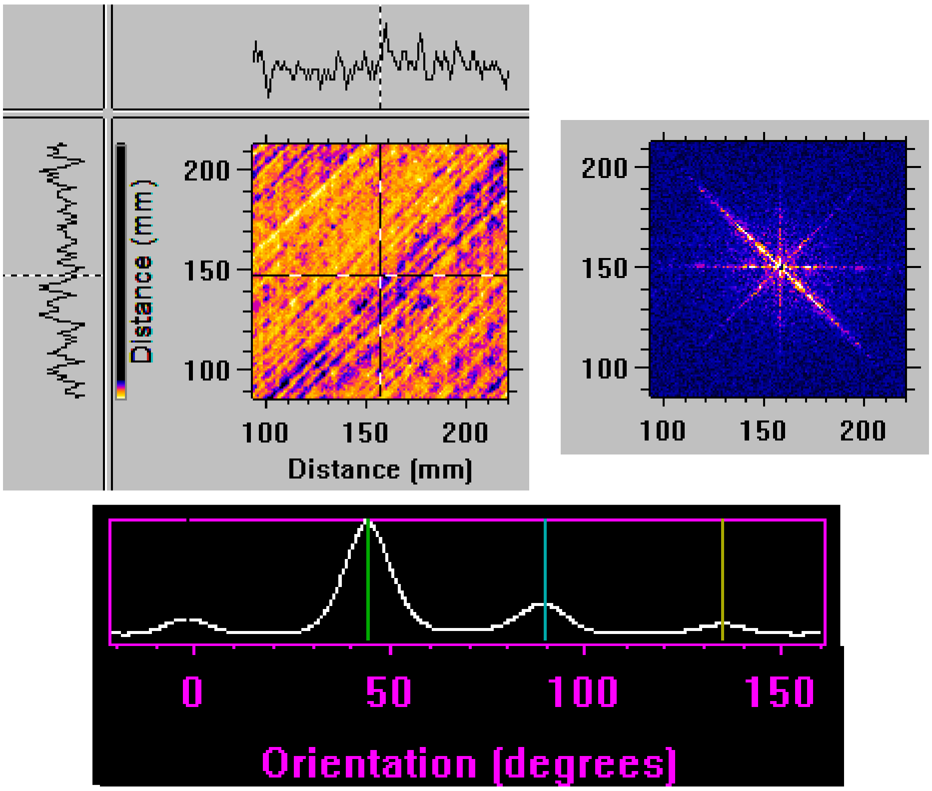

Figure H-1. Typical layer C-scan (left) from the centre of the 7th ply in a 16-ply stack – a 45º ply – and its corresponding 2D-FFT (right). The angular power distribution from this 2D-FFT is shown at the bottom.

H.2 Peak angle measurement

The basic methodology for converting C-scan images of fibre tows or B-scan images of plies has been thoroughly covered in previous chapters. Part of the process is a polar transformation of the 2D Fast Fourier Transform (FFT) output image into an angular power distribution. Additional processing of the polar transform is required for two purposes: to remove angular bias and to remove the effects of stitching in the composite. Both of these are covered in previous chapters. The system being assessed here includes this additional processing.

H.2.1 Angular accuracy measuring equally-spaced line orientation

Each of the following sources of systematic uncertainty will be presented as a function of angle, having been assessed for lines spaced at any angle from 0º to 45º. As the image and the 2D-FFT are presumed to be approximately square, with square pixels (unity aspect ratio), the angles from 45º to 90º can be assumed to have a symmetrical dependence, and so on for angles up to 180º.

The measurements made for the other sources of uncertainty below show that, provided there are enough points in the image (>100 x 100), there are enough lines (fibre tows) across the image (>20), and the spacing is *not* uniform, then the systematic uncertainty due purely to angular variation is less than ±0.25º (smaller than can be measured using a 0.25º resolution).

If the line spacing is uniform and the lines are a sine-wave function, the 2D-FFT will contain just two narrow peaks (Figure H-2 left) – symmetrically, either side of the centre (zero frequency) point, multiplied by 0º/90º sinc-function (sin(x)/x) structure representing the 2D-FFT of the window of the whole image (Figure H-2 centre). For this reason, constant spacing is not necessarily a truly representative distribution of lines because it does not have a 2D-FFT that is similar to that of a C-scan (as in Figure H-1). It may be better to have variable spacing, preferably random, to spread the response in the 2D-FFT along a line from the centre (Figure H-2 right) so this will be investigated in the next section.

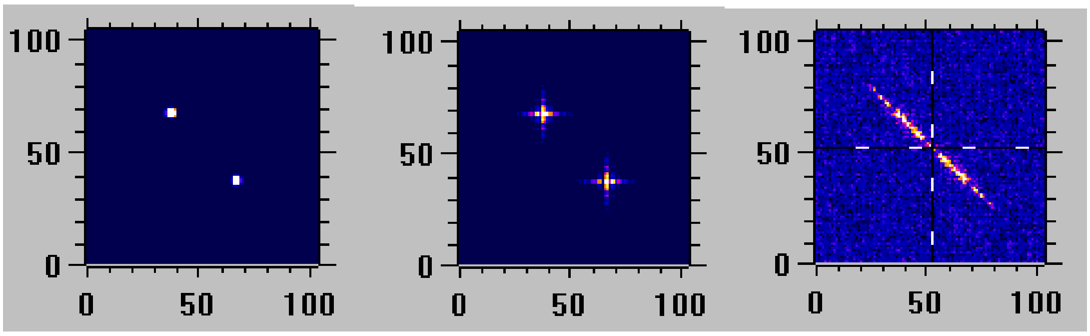

Figure H-2. 2D-FFT from constant spacing lines using a 100% Hanning window (left) or a 20% Hanning window (centre) and 2D-FFT from pseudo-random spacing (right)

The accuracy of angular measurement on 100% and 20% Hanning-windowed images of equally spaced lines has been investigated for lines at every 0.25º angle from 0º to 45º in Figure H-3. If the accuracy is taken as the peak-to-peak variation in the error, it is better than ±0.25º if there are at least 106 x 106 pixels (this is not necessarily a minimum number of pixels) and it improves with an increasing number of pixels in the region of the image used for the analysis.

Zero padding to a greater number of pixels prior to FFT analysis was found to make negligible difference to the above angular distribution of errors.

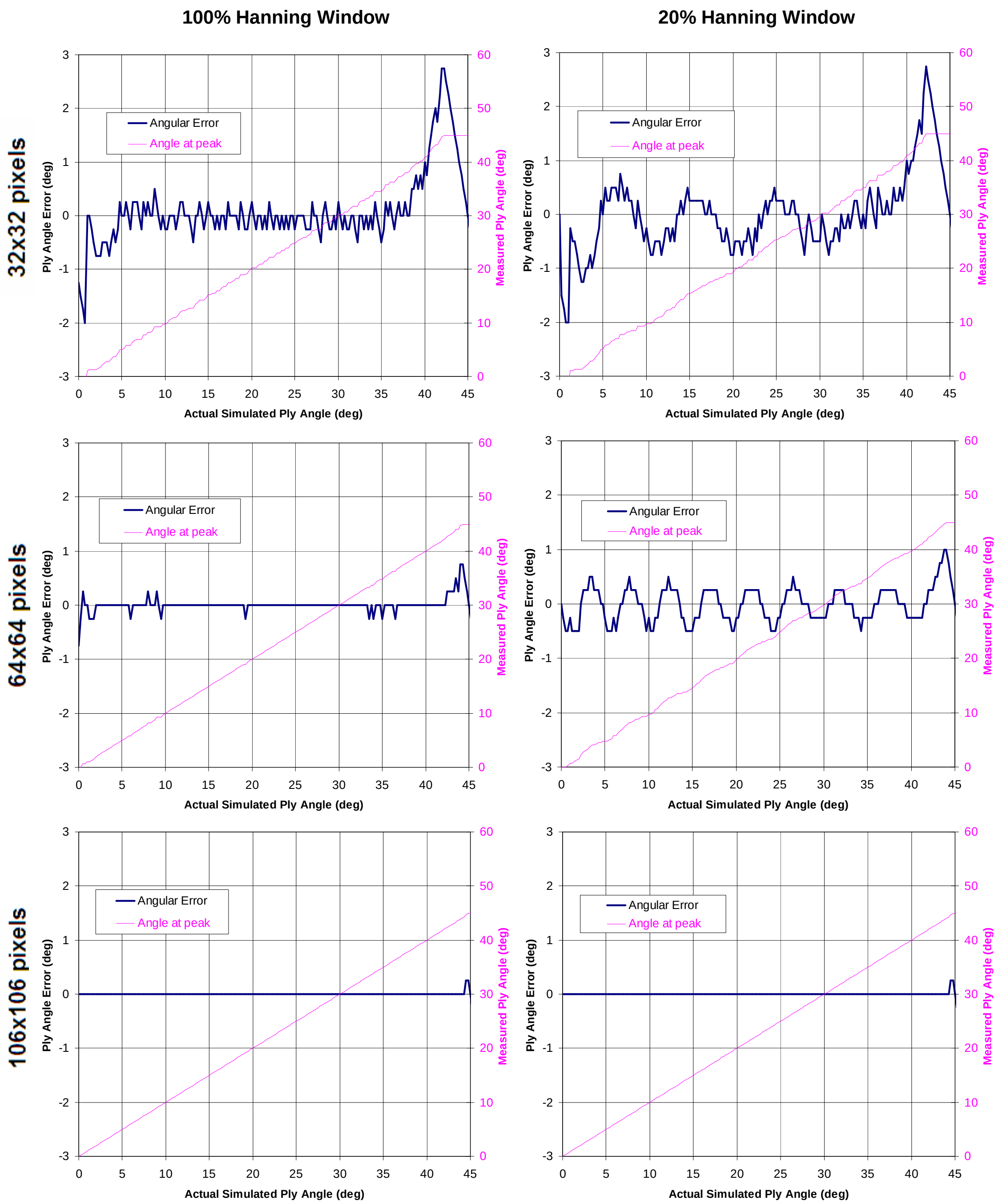

Figure H-3. Graphs of measured ply angle (pink) and the error in this measurement (blue) as a function of the angle of the 5-mm spaced simulated fibre tows, for regions: 32 x 32 pixels (top), 64 x 64 pixels (middle) and 106 x 106 pixels (bottom), using a Hanning window over 100% (left), or only over 20% (right), of the region. The increment between simulated angles was 0.25º.

H.2.2 Angular accuracy for variably spaced line orientation

The above analysis is artificial in that C-scans of fibre tows, in addition to the basic fibre-tow spacing, actually demonstrate other effects which can be categorised as a) sub-harmonics of the fundamental tow spacing, b) interference with adjacent plies of different angles, and c) other spatial noise.

A more realistic simulation of a real C-scan has been produced, which can be rotated to any desired angle. This uses harmonics and sub-harmonics to try to produce a realistic spread of spatial frequencies in the 2D-FFT, and it also adds random noise to the phase of the spatial frequencies to try to simulate the noise seen in real C-scans. An example of such a simulated C-scan and its 2D-FFT is shown in comparison with real measured ultrasonic versions in Figure H-4.

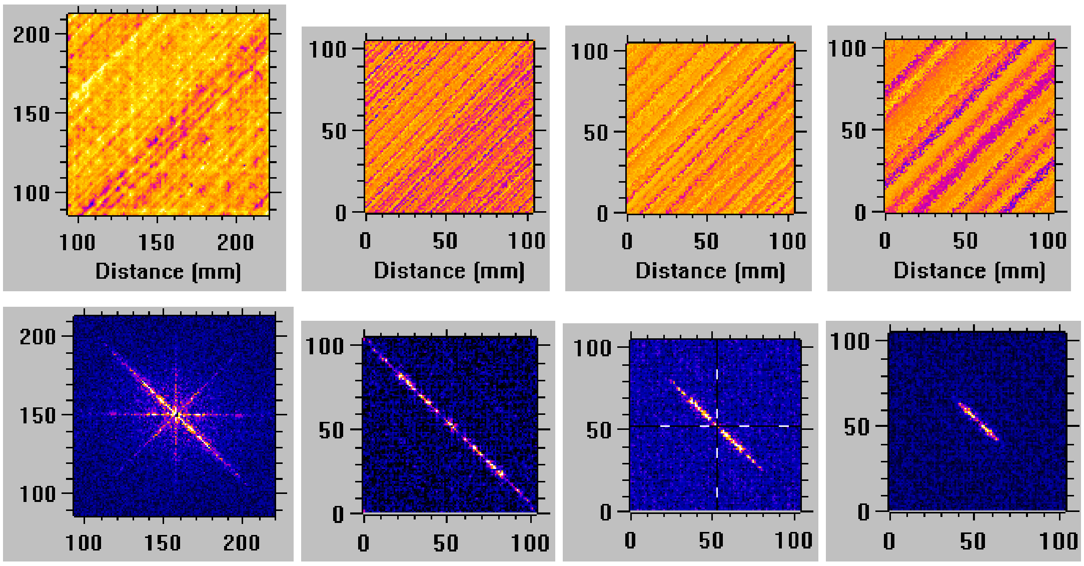

Real 45 degree ply **2.5 mm fibre tows** **5 mm fibre tows** **10 mm fibre tows**

Figure H-4. A real C-scan (top-left) with its 2D-FFT (bottom-left) and simulated variable-spacing C-scans (top) with their 2D-FFTs (bottom). Different fibre-tow spacings are illustrated for simulated C-scans: (left to right) 2.5, 5 and 10 mm.

The accuracy of angular measurements on these simulated variable-spacing C-scans is illustrated in Figure H-5 and suggests that, if an accuracy of ±0.25º is to be achieved, the region used for angular analysis should include at least 20 fibre tows and 100 x 100 pixels. Therefore, a scan step size of between 1/2 and 1/5 of the fibre-tow spacing is recommended, giving 2 to 5 pixels per fibre tow, and a region with at least 100 x 100 pixels should be used for analysis.

The introduction of spatial noise into the simulated image did not adversely affect the accuracy at the relatively low noise levels used, although there obviously would be an effect for very high noise levels.

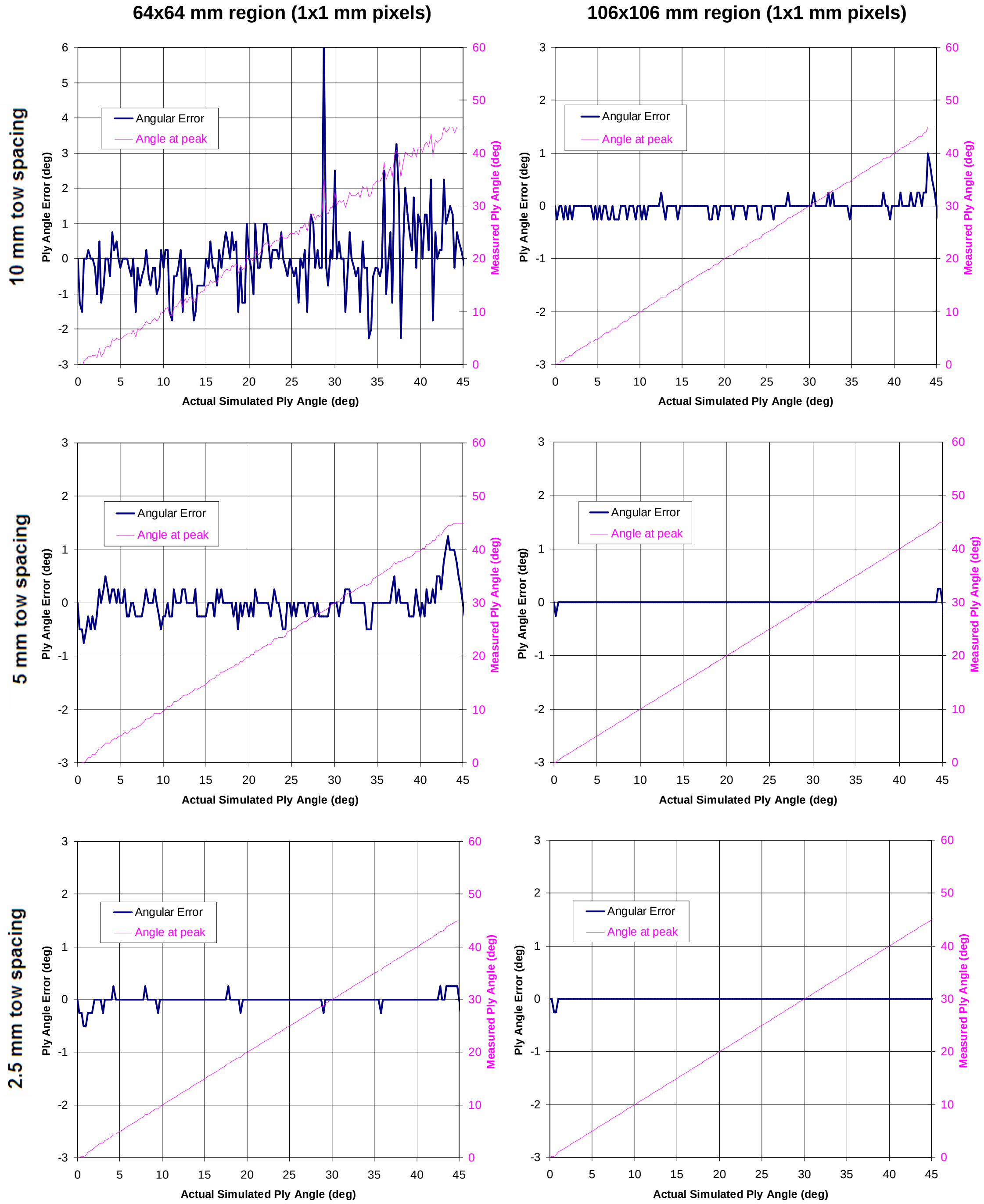

Figure H-5. Graphs of measured ply angle (pink) and the error in this measurement (blue) as a function of the angle of variably-spaced simulated fibre tows, for regions: 64 x 64 mm (left) and 106 x 106 mm (right), using a Hanning window over 20% of the region. Fundamental fibre-tow spacings were 10 mm (top), 5 mm (middle) and 2.5 mm (bottom). The increment between simulated angles was 0.25º.

The accuracies demonstrated in Figure H-5 have been extended with further measurements to give Table H-1. All sizes are scaled to the fibre-tow spacing, giving box size in numbers of fibre tows, and pixel size as a fraction of the fibre-tow spacing.

Pixels per fibre tow	Box size (# fibre tows)			
	40	20	10	5
10			±1º	±5º
5		±0.25º	±1º	±5º
4		±0.25º	±0.5º	±3º
3		±0.5º	±1.75º	±4º
2.5	±0.25º	±0.5º	±1.5º	

Table H-1. Accuracies as a function of pseudo-random simulated fibre-tow spacing and the box size used for in-plane waviness measurements.

H.3 In-plane waviness accuracy

The above analysis suggests that in order to obtain ±0.25º accuracy, a region at least 100x100 pixels containing at least 20 fibre tows should be used. This is likely to be feasible for ply stacking sequence analysis where the average fibre orientation over a substantial region is required. However, it is rarely possible for in-plane waviness mapping, where a small box is raster-scanned over each C-scan image and the size of the box needs to be small enough to minimise averaging of orientation over the waviness. In order to compromise between absolute accuracy of orientation measurement and averaging out the waviness, it is necessary to use a box that will contain fewer than the optimum 100 x 100 pixels and also fewer than 20 fibre tows. To determine the best compromise box size and pixel size for in-plane waviness, it is necessary to consider how the maximum expected waviness is linked to fibre tow size and how the accuracy of the fibre angle measurement depends on box size as a function of wrinkle wavelength. For the purposes of the analysis in Table H-2, the minimum expected in-plane waviness wavelength was equal to n fibre-tow spacings.

The box needs to be positioned exactly over the peak angle in order to measure it accurately. Increasing the overlap between adjacent boxes improves the chances of accurate positioning over the peak angle. To demonstrate this, 50% and 75% overlaps were used to assess the in-plane waviness in Figure H-6.

n, fibre tows per wavelength	Box size (# fibre tows)			
	20	10	5	3
40		-3.5º ±0.5º	±1º	+3º ±1º
20		-3.5º ±1º	-2º ±2º	+1º ±4º
10		-3º ±1º	-2º ±2º	-3º ±4º

Table H-2. Errors and uncertainties as a function of box size and wrinkle wavelength for simulated sinusoidal in-plane waviness and 5 pixels per fibre-tow width. Values are for plies of 0º/45º/90º simulated using the pseudo-random method with noise.

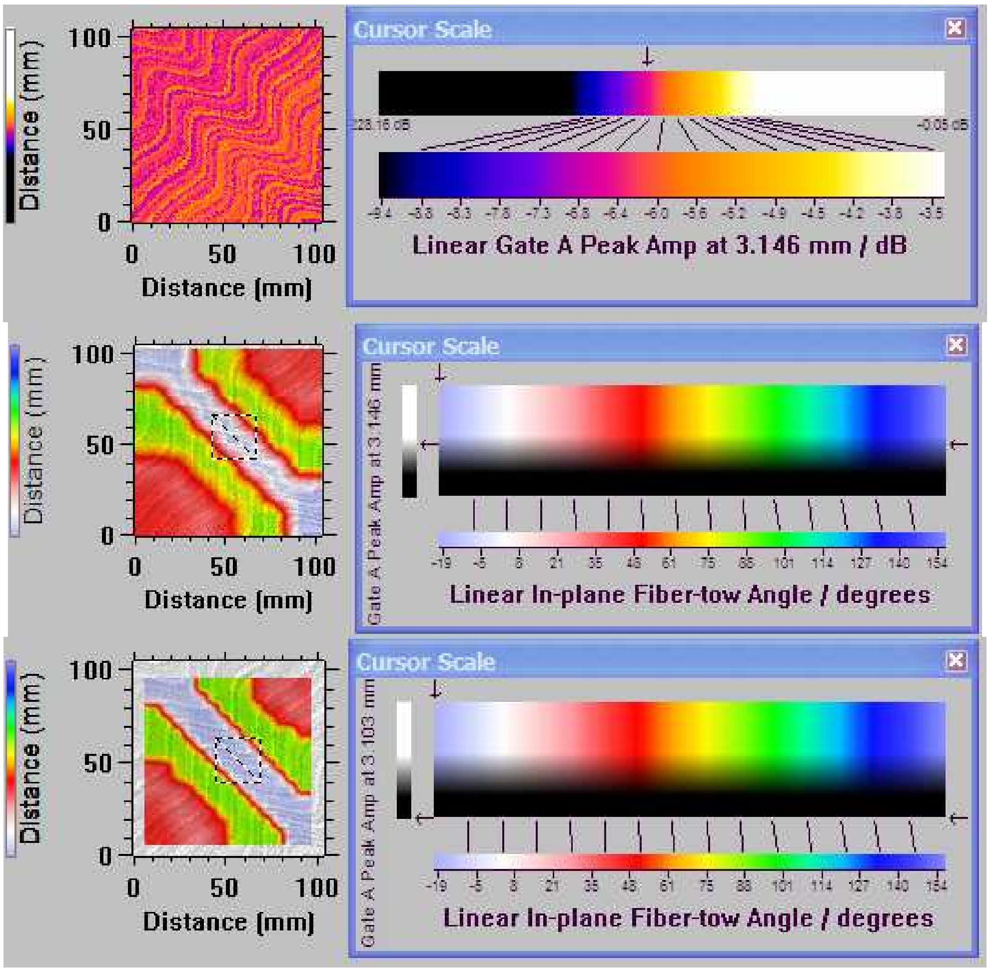

Figure H-6. An example of the in-plane waviness analysis of a simulated in-plane wave in a 45º ply of amplitude 13 mm, wavelength 50 mm, envelope half-width 30 mm, step size 1 mm, box size 25 x 25 mm and fibre-tow spacing 5 mm. Simulated C-scan (top), combined C-scan and in-plane fibre angle scan with 50% overlap (middle) and with 75% overlap (bottom).

The peak deviation from 45º occurs at the centre of the waviness, where the Gaussian envelope is unity. The wave is a sine wave with 13 mm amplitude and Equation G-2 in Appendix G gives a peak angular deviation of -58.5º for a 50 mm wavelength, -39.2º for a 100 mm wavelength or -22.2 for a 200 mm wavelength. Errors and uncertainties given in Table H-2 were determined from plots as shown in Figure H-7. An underestimate in the calculated peak deviation is caused by a combination of the box not being positioned exactly over the steepest slope in the wave, and the box averaging over portions of the wave with reduced slope. Note that the measurement is stored in an 8-bit bitmap with 256 levels spread over 180°, giving digitisation noise of around ±0.7°

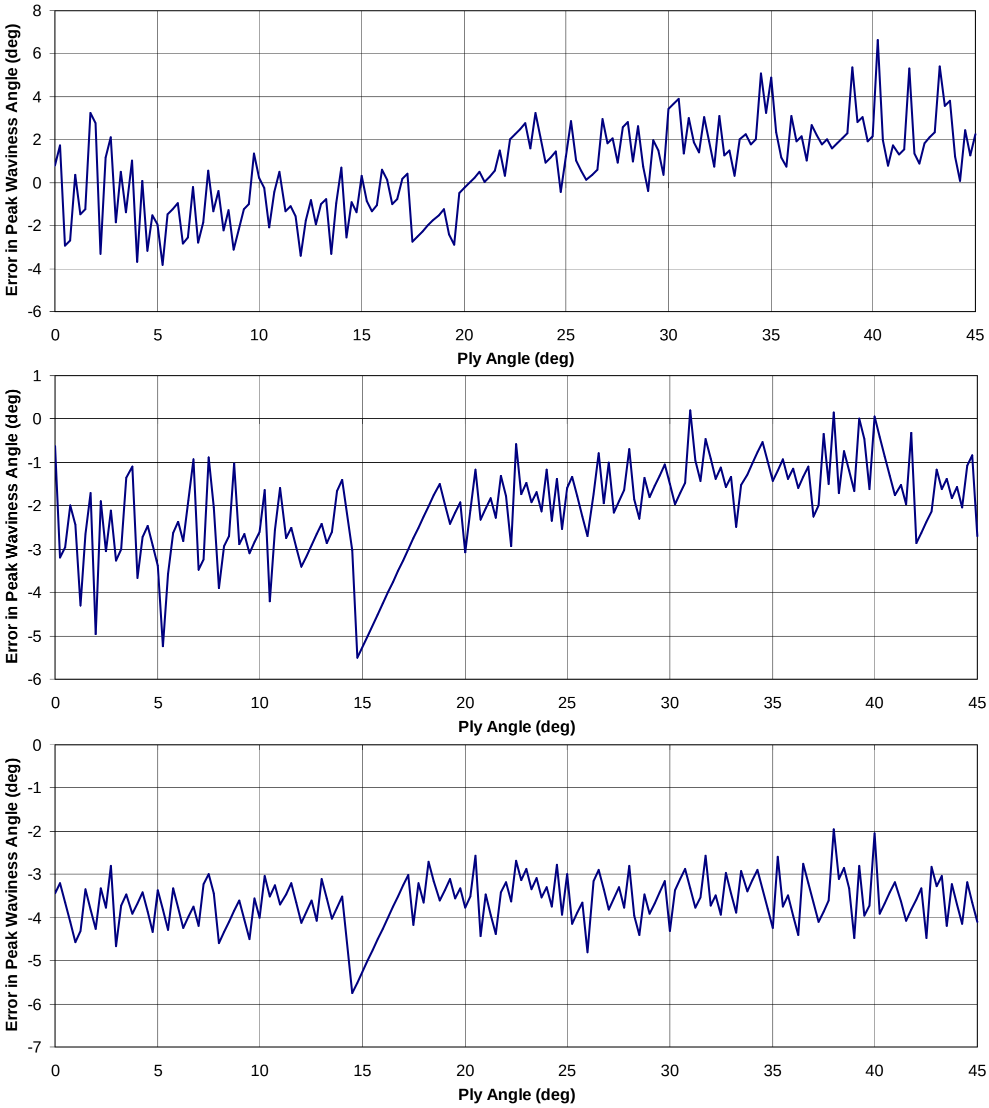

Figure H-7. Error in measuring the peak angular deviation for 13 mm amplitude, 100 mm wavelength waviness with 5 mm fibre tow width and box sizes of 15 x 15 mm (top), 25 x 25 mm (middle) and 50 x 50 mm (bottom).

H.4 Ultrasonic C-scan generation

H.4.1 Smoothing through spatial averaging

Spatial averaging can be simulated easily by introducing smoothing of each image prior to angular analysis. The results for averaging of 5 mm tow spacing (variable spacing) scans over spot sizes up to 10 mm are shown in Figure H-8. The inaccuracies due to spatial averaging are no greater than ±0.25º. Whilst this has not been tested for real ultrasonic spatial averaging, there is no reason to suspect any greater inaccuracies than for these simulated experiments.

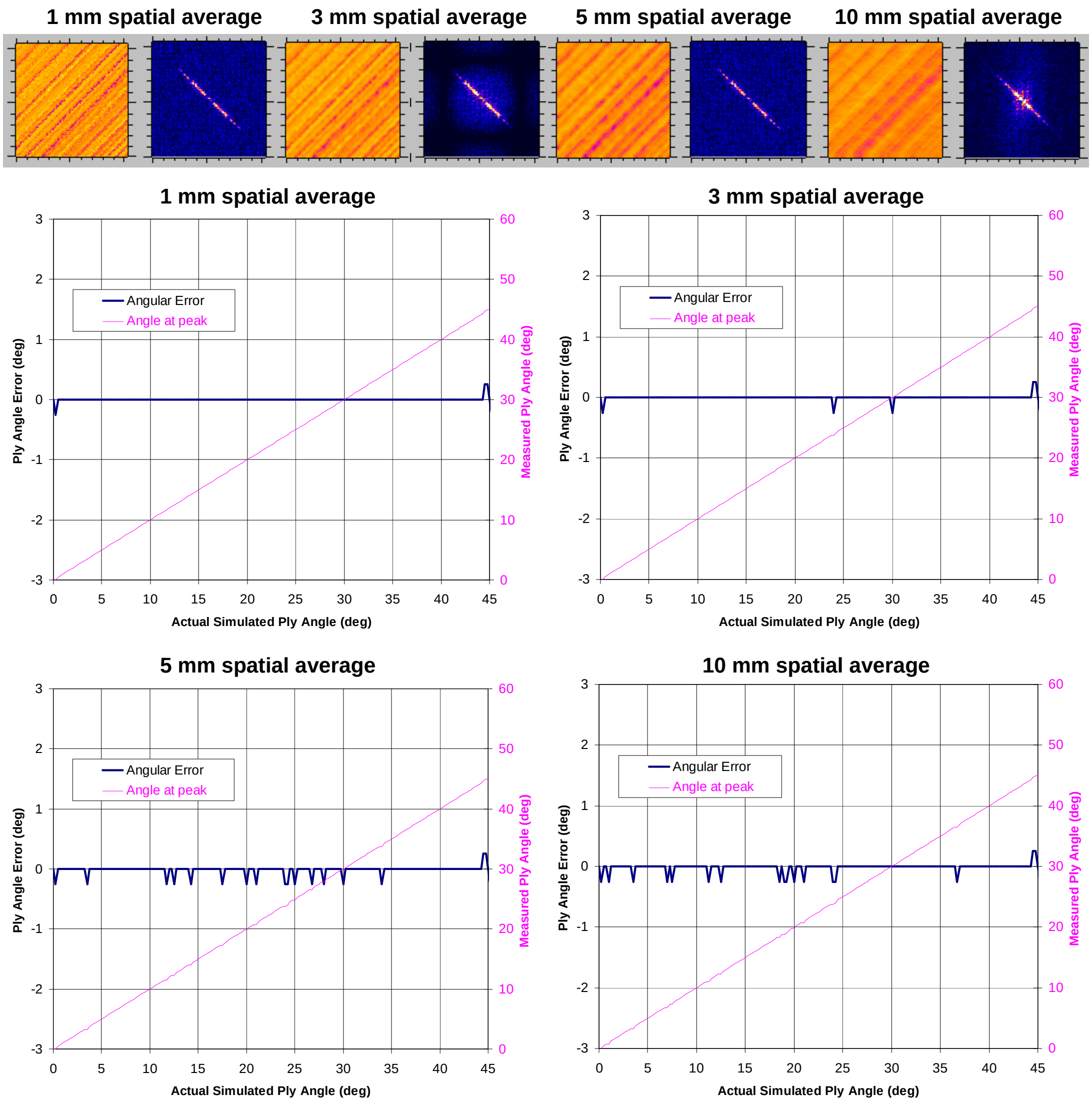

Figure H-8. Graphs of measured ply angle (pink) and the measurement error (blue) as a function of the angle of variably-spaced simulated fibre tows for C-scans (top row) that have been spatially-averaged over spot sizes of 1 mm (top-left), 3 mm (top-right), 5 mm (bottom-left) and 10 mm (bottom-right).

H.4.2 Presence of lines from adjacent plies at other angles

Whilst adjacent plies cause small peaks at other angles, they should only affect the accuracy of the measurement of the dominant peak if they are close in angle. As adjacent ply orientations differ by at least 45º, it is not expected that any inaccuracies will result.

H.4.3 Other depth-dependent effects

The most obvious depth-dependent effects are those in the above two sub-sections: spatial averaging over the beam profile, and leakage of angles from adjacent plies. The latter problem will be exacerbated near the back-wall echo depth where the broad-band back-wall reflection interferes with the ply resonances (see Figure H-9). However, it is still felt that the main errors caused will be in mistaking which orientation corresponds to which ply, rather than an inaccurate measurement of the actual angle of the ply orientation.

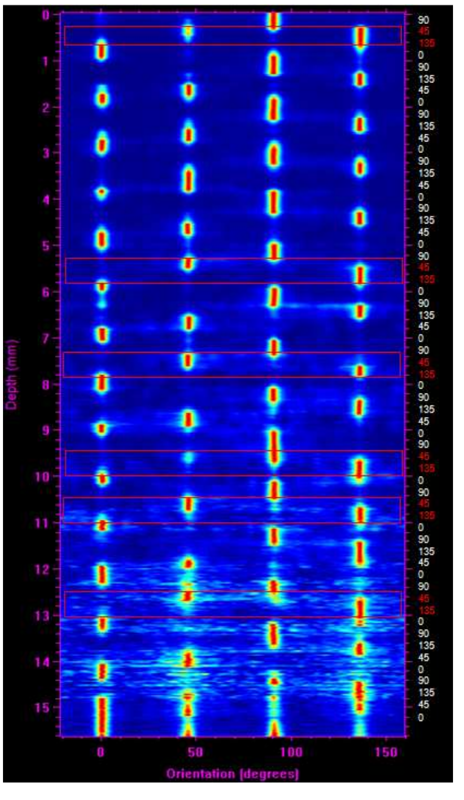

Figure H-9. An example of a 60-ply 15 mm thick composite showing the confusing response near the back-wall echo (bottom of image) and that the angular width of each ply's peak orientation does not appear to broaden significantly with depth in the structure.

As the ultrasound propagates through the material there is more visco-elastic attenuation of the higher frequencies, and the ply resonance frequency itself becomes a band-gap in the incident spectrum. The reduction in the peak frequency should only result in broadening of the beam and greater spatial averaging, similar to the variations in focal beam profiles that would be expected. Loss of the resonant frequencies of the plies does not seem to have a marked effect, even through 60 or more plies, with the width of the angular peaks being maintained through the structure (see Figure H-9).

H.4.4 Waviness in the lines

Waviness in the lines in a region of an image can be the source of uncertainty in a measurement of average peak orientation within that region. The method can at best measure the average or most common orientation within the region and any waviness will cause a broadening of the peak at that orientation.

To investigate this effect, waviness was introduced to simulated C-scans with pseudo-random tow spacing, as used above, and the results are shown in Figure H-10.

It can clearly be seen in the 2D-FFTs that the wrinkle introduces a broader range of angles in the region being analysed and this directly affects the accuracy with which the average ply orientation can be measured. However, a wrinkle of just 0.5 mm amplitude and 60 mm wavelength has a maximum angular deviation of 3.0º, which is much greater than the allowable 1.8º for a fibre wrinkle in some current OEM specifications.

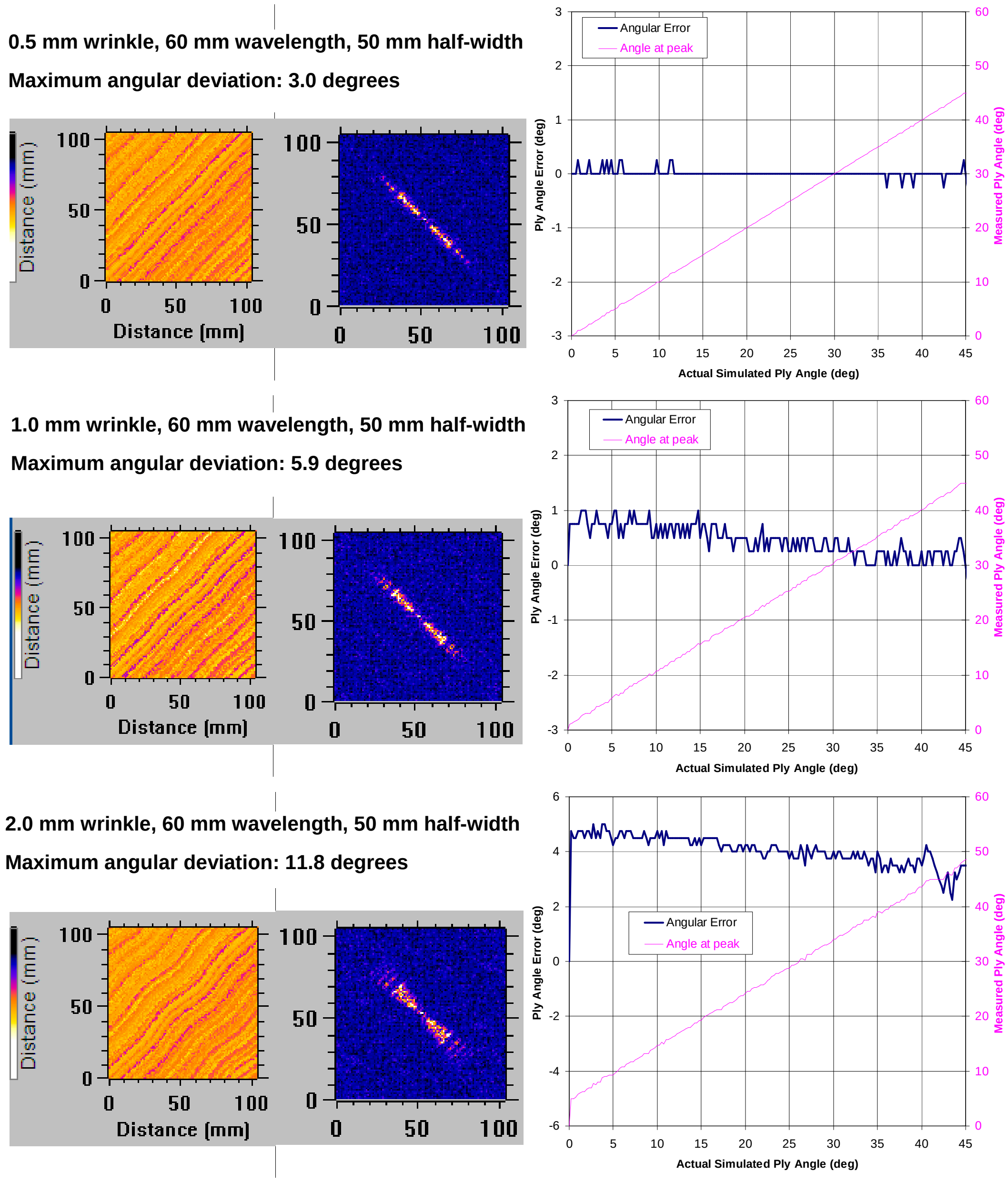

Figure H-10. C-scans (left), 2D-FFTs (middle) and angular accuracies (right) as the amplitude of wrinkle increases from 0.5 mm (top) to 2 mm (bottom), with a 60 mm wrinkle wavelength and wrinkle half-width of 50 mm.

H.5 Out-of-plane wrinkling

The accuracy of out-of-plane wrinkling measurements depends on the wrinkle wavelength and the box size used to define the analysis regions. As with in-plane waviness, the box needs to be narrow in order not to spatially-average the peak angle, but it needs to be as many pixels wide as possible to improve the accuracy of the measurement of angle. Thus a small incremental step size in the original scan is beneficial as this maximises the number of pixels per wrinkle wavelength.

The number of plies included in the box height is also important. Figure H-11 shows the benefit of including four rather than two plies, for four different box widths: 20, 50, 75 and 100 pixels, just measuring straight lines at a range different angles.

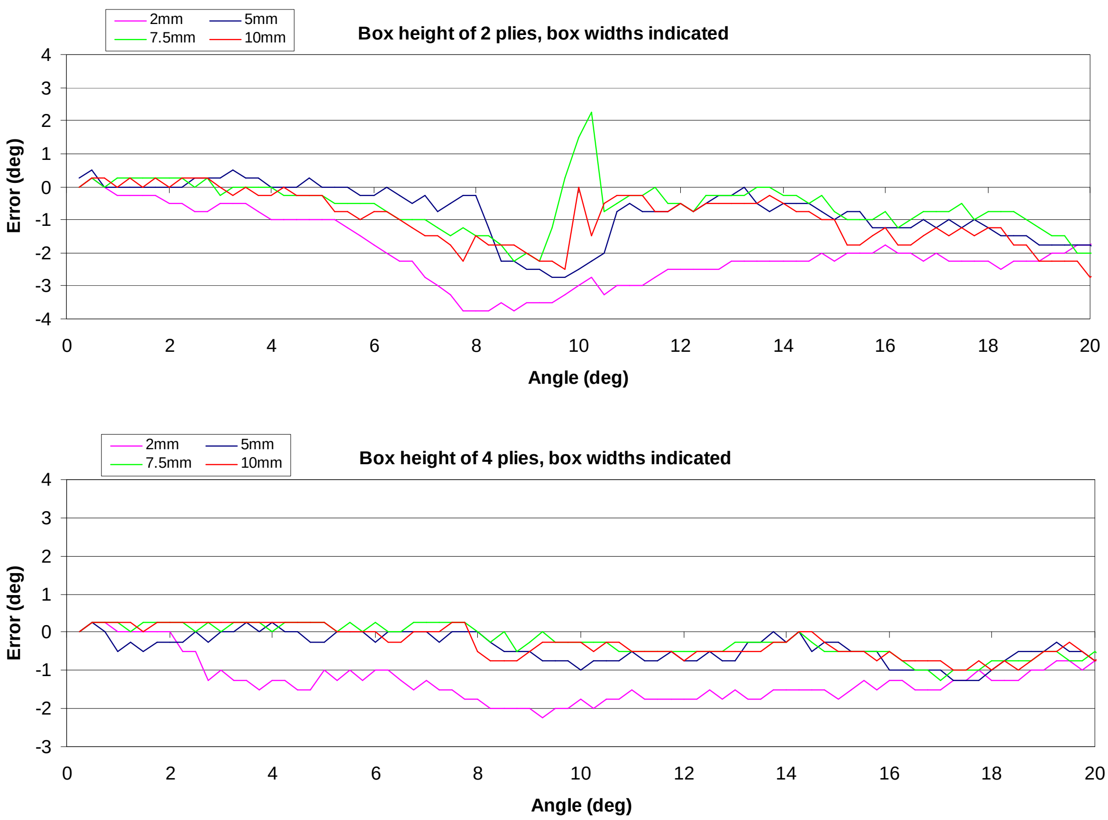

Figure H-11. Errors in angular measurement as a function of ply angle for different box widths (10 pixels per millimetre) and a box height including two plies (top) or four plies (bottom).

H.6 Fibre orientation accuracy summary

This appendix has summarised the work to date on the accuracy of the fibre orientation methods. It is work in progress in an iterative fashion in that, as accuracies are assessed, a greater insight is gained, leading to improvements in the algorithms. This then requires a further accuracy assessment and the cycle repeats.

It has been shown that the ply stacking sequence method has potential for the greatest angular accuracy because of the ability to use a large number of pixels in the analysis region. For waviness and wrinkling this region needs to be smaller in order to plot just localised orientation. Reducing the size of the analysis region results in poorer accuracies, but there is potential to reduce the incremental step size in scans and increase the full-waveform digitisation sampling rate in order to increase the number of pixels in the analysis region.